

REPORT DOCUMENTATION PAGE					<i>Form Approved</i> OMB No. 0704-0188	
The public reporting burden for this collection of information is estimated to average 1 hour per response, including the time for reviewing instructions, searching existing data sources, gathering and maintaining the data needed, and completing and reviewing the collection of information. Send comments regarding this burden estimate or any other aspect of this collection of information, including suggestions for reducing the burden, to Department of Defense, Washington Headquarters Services, Directorate for Information Operations and Reports (0704-0188), 1215 Jefferson Davis Highway, Suite 1204, Arlington, VA 22202-4302. Respondents should be aware that notwithstanding any other provision of law, no person shall be subject to any penalty for failing to comply with a collection of information if it does not display a currently valid OMB control number. PLEASE DO NOT RETURN YOUR FORM TO THE ABOVE ADDRESS.						
1. REPORT DATE (DD-MM-YYYY) 11-05-2015		2. REPORT TYPE Final			3. DATES COVERED (From - To) 25 Apr 13 – 24 Apr 15	
4. TITLE AND SUBTITLE Electrochemical investigations on graphene and lithium phthalocyanine as catalysts for reversible oxygen reduction reaction in Li-O ₂ cells				5a. CONTRACT NUMBER FA2386-13-1-4006		
				5b. GRANT NUMBER Grant AOARD-134006 13RSZ011		
				5c. PROGRAM ELEMENT NUMBER		
6. AUTHOR(S) Prof. Munichandraiah Nookala				5d. PROJECT NUMBER		
				5e. TASK NUMBER		
				5f. WORK UNIT NUMBER		
7. PERFORMING ORGANIZATION NAME(S) AND ADDRESS(ES) Indian Institute of Science Department of Inorganic and Physical Chemistry Bangalore 560 012 India					8. PERFORMING ORGANIZATION REPORT NUMBER N/A	
9. SPONSORING/MONITORING AGENCY NAME(S) AND ADDRESS(ES) AOARD UNIT 45002 APO AP 96338-5002					10. SPONSOR/MONITOR'S ACRONYM(S) AFRL/AFOSR/IOA(AOARD)	
					11. SPONSOR/MONITOR'S REPORT NUMBER(S) AOARD-134006	
12. DISTRIBUTION/AVAILABILITY STATEMENT Distribution A: Approved for public release. Distribution is unlimited.						
13. SUPPLEMENTARY NOTES						
14. ABSTRACT The theoretical energy density of Li-air battery is close to that of gasoline. One hurdle to implementation is electrochemistry of oxygen in non-aqueous electrolytes, including development of a suitable catalyst for reversible oxygen electrode for long cycle-life. Several reduced graphene oxide (RGO) preparations were tested in both aqueous and non-aqueous electrolytes using cyclic voltammetry and rotating disk electrode techniques. Studies were carried out using silver nano-particles (Ag-RGO), as well as gold (Au-RGO), palladium (Pd-RGO), iridium (Ir-RGO) and polypyrrole (PPY-RGO). Prototype cells were assembled and tested in charge and discharge at several current densities. Initial cycling shows a decrease in capacity, stabilizing after approximately 30 charge-discharge cycles. The results indicate that RGO based catalysts are appropriate for deriving high discharge capacity from rechargeable Li-O ₂ cells.						
15. SUBJECT TERMS lithium air battery, Graphene, Chemistry, Electrochemical devices						
16. SECURITY CLASSIFICATION OF:			17. LIMITATION OF ABSTRACT SAR	18. NUMBER OF PAGES 58	19a. NAME OF RESPONSIBLE PERSON David Hopper, Lt Col, USAF, Ph.D.	
a. REPORT U	b. ABSTRACT U	c. THIS PAGE U			19b. TELEPHONE NUMBER (Include area code) +81-3-5410-4409	

Report Documentation Page			Form Approved OMB No. 0704-0188		
Public reporting burden for the collection of information is estimated to average 1 hour per response, including the time for reviewing instructions, searching existing data sources, gathering and maintaining the data needed, and completing and reviewing the collection of information. Send comments regarding this burden estimate or any other aspect of this collection of information, including suggestions for reducing this burden, to Washington Headquarters Services, Directorate for Information Operations and Reports, 1215 Jefferson Davis Highway, Suite 1204, Arlington VA 22202-4302. Respondents should be aware that notwithstanding any other provision of law, no person shall be subject to a penalty for failing to comply with a collection of information if it does not display a currently valid OMB control number.					
1. REPORT DATE 11 MAY 2015		2. REPORT TYPE Final		3. DATES COVERED 25-04-2013 to 24-04-2015	
4. TITLE AND SUBTITLE Electrochemical investigations on graphene and lithium phthalocyanine as catalysts for reversible oxygen reduction reaction in Li-O2 cells			5a. CONTRACT NUMBER FA2386-13-1-4006		
			5b. GRANT NUMBER		
			5c. PROGRAM ELEMENT NUMBER		
6. AUTHOR(S) Munichandraiah Nookala			5d. PROJECT NUMBER		
			5e. TASK NUMBER		
			5f. WORK UNIT NUMBER		
7. PERFORMING ORGANIZATION NAME(S) AND ADDRESS(ES) Indian Institute of Science, Department of Inorganic and Physical Chemistry, Bangalore 560 012, India, IN, 560012			8. PERFORMING ORGANIZATION REPORT NUMBER N/A		
9. SPONSORING/MONITORING AGENCY NAME(S) AND ADDRESS(ES) AOARD, UNIT 45002, APO, AP, 96338-5002			10. SPONSOR/MONITOR'S ACRONYM(S) AFRL/AFOSR/IOA(AOARD)		
			11. SPONSOR/MONITOR'S REPORT NUMBER(S) AOARD-134006		
12. DISTRIBUTION/AVAILABILITY STATEMENT Approved for public release; distribution unlimited					
13. SUPPLEMENTARY NOTES					
14. ABSTRACT The theoretical energy density of Li-air battery is close to that of gasoline. One hurdle to implementation is electrochemistry of oxygen in non-aqueous electrolytes, including development of a suitable catalyst for reversible oxygen electrode for long cycle-life. Several reduced graphene oxide (RGO) preparations were tested in both aqueous and non-aqueous electrolytes using cyclic voltammetry and rotating disk electrode techniques. Studies were carried out using silver nano-particles (Ag-RGO), as well as gold (Au-RGO), palladium (Pd-RGO), iridium (Ir-RGO) and polypyrrole (PPY-RGO). Prototype cells were assembled and tested in charge and discharge at several current densities. Initial cycling shows a decrease in capacity, stabilizing after approximately 30 charge-discharge cycles. The results indicate that RGO based catalysts are appropriate for deriving high discharge capacity from rechargeable Li-O2 cells.					
15. SUBJECT TERMS lithium air battery, Graphene, Chemistry, Electrochemical devices					
16. SECURITY CLASSIFICATION OF:			17. LIMITATION OF ABSTRACT Same as Report (SAR)	18. NUMBER OF PAGES 58	19a. NAME OF RESPONSIBLE PERSON
a. REPORT unclassified	b. ABSTRACT unclassified	c. THIS PAGE unclassified			

**Electrochemical investigations on graphene and lithium phthalocyanine as
catalysts for reversible oxygen reduction reaction in Li-O₂ cells**

(FA2386-13-1-4006)

Final Report

Submitted to:

**Asian Office of Aerospace Research and Development
7-23-17 Roppongi, Minato-Ku
Tokyo 160-0032
Japan**

By:

**Indian Institute of Science
Bangalore -560012, India
(Investigator: Munichandraiah Nookala)**

Final Report for AOARD Grant FA2386-13-1-4006

Electrochemical Investigations on graphene and lithium phthalocyanine as catalysts for reversible oxygen reduction reaction in Li-O₂ cells

April 2015

Name of Principal Investigators:	Prof. Munichandraiah Nookala
- e-mail address :	muni@ipc.iisc.ernet.in
- Institution :	Indian Institute of Science, INDIA
- Mailing Address :	Department of Inorganic and Physical
-	Chemistry, Indian Institute of Science, Bangalore- 560012, India
- Phone :	+91-80-2293-3183
- Fax :	+91-80-2360-0683, 2360-1552
Period of Performance:	April 2013 - April 2015

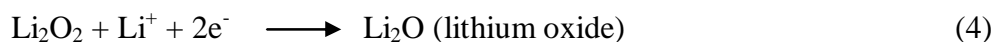
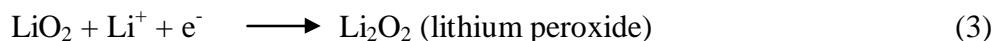
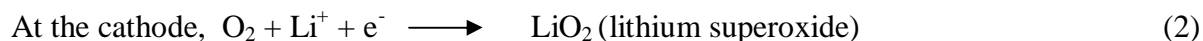
Abstract:

It is expected that Li-air battery has the highest energy density among all existing rechargeable battery systems. Literature reports suggest that the theoretical energy density of Li-air battery is close to that of gasoline. Thus, if successfully developed, rechargeable Li-air battery will be a suitable substitute for gasoline for electric vehicles. The research and development work is at initial stages worldwide at present. Electrochemistry of oxygen in non-aqueous electrolytes is one of the crucial factors. Development of a suitable catalyst for reversible oxygen electrode for long cycle-life is important. Silver nanoparticles anchored reduced graphene oxide (Ag-RGO) is

prepared by simultaneous reduction of graphene oxide and Ag^+ ions in an aqueous medium by ethylene glycol as the reducing agent. Ag particles of average size of 4.7 nm are uniformly distributed on the RGO sheets. Oxygen reduction reaction (ORR) is studied on Ag-RGO catalyst in both aqueous and non-aqueous electrolytes by using cyclic voltammetry and rotating disk electrode techniques. As the interest in non-aqueous electrolyte is to study the catalytic performance of Ag-RGO for rechargeable Li-O_2 cells, these cells are assembled and characterized. Li-O_2 cells with Ag-RGO as the oxygen electrode catalyst are subjected to charge-discharge cycling at several current densities. A discharge capacity of $11,950 \text{ mAh g}^{-1}$ ($11.29 \text{ mAh cm}^{-2}$) is obtained initially at low a current density. Although there is a decrease in capacity on repeated discharge-charge cycling initially, a stable capacity is observed for about 30 cycles. Similar studies are carried out using Au-RGO, Pd-RGO, Ir-RGO and PPY-RGO (PPY: polypyrrole). The results indicate that RGO based catalysts are appropriate for deriving high discharge capacity from rechargeable Li-O_2 cells.

1. INTRODUCTION

In Li-air battery, Li metal is stored within the cell and oxygen is consumed from air. The cell functions in a non-aqueous electrolyte by oxidation of Li metal to Li^+ ion and oxygen absorbed from air by the cathode undergoes reduction to superoxide, peroxide or oxide. The corresponding electrochemical reactions are given below.



The electrochemical properties of the oxygen electrode largely influence the performance of Li-air cells. Carbon is usually used as the substrate for oxygen reaction. The physical structure of carbon such as surface area, porosity, wettability, etc., and the catalyst influence electrochemistry of reversible oxygen electrode reaction. After screening several carbon samples, it is found that an activated carbon has surface area as high as $1500 \text{ m}^2/\text{g}$ and the performance of air-electrodes made of this carbon is good. This carbon sample is used for fabrication of air electrodes in these investigations, as reported below.

Research activities on Li- O_2 (or, Li-air) battery system have become intensive in recent years. This is because of an extremely high theoretical energy density ($11.68 \text{ kWh kg}^{-1}$) of this battery system, which is anticipated to be a clean and environmental friendly substitute for

gasoline. In air-breathing mode of operation, O₂ is received free of cost from the atmosphere and there is no need for its storage inside the cell. Development of primary Li-air cells may be less tedious than the development of rechargeable cells. Development of rechargeable Li-air cells involves several issues related to the negative Li electrode, the positive O₂ electrode as well as the electrolyte. Among these problems, studies on rechargeable O₂ electrode kinetics in non-aqueous electrolytes are important. Development of suitable electrode configuration and an appropriate catalyst, which allow both O₂ reduction and its evolution with fast kinetics and high efficiency, are the present-day challenges in research activities in this area.

Several catalysts have been evaluated for rechargeable O₂ electrode in non-aqueous electrolytes. Abraham and Jiang reported a polymer electrolyte based rechargeable Li-O₂ cell employing cobalt phthalocyanine as the catalyst for O₂ electrode. The cell discharge voltage was in the range 2.50-3.00 V and charge voltage in 3.50-4.00 V range. Cells were charged and discharged at current densities of 0.05 and 0.10 mA cm⁻², respectively. Capacity values close to 600 mAh g⁻¹ were reported. These studies were followed by the report of Ogasawara *et al*, which described using of electrolytic manganese dioxide as the catalyst. Flat curves of discharge and charge voltages at 2.70 and 4.20 V, respectively, were reported with an initial discharge capacity of 1000 mAh g⁻¹ at a specific current of 50 mA g⁻¹. There was a gradual decrease in capacity on repeated charge-discharge cycling, and about 600 mAh g⁻¹ was reported at the end of 50 cycles. Subsequently, several other catalysts for O₂ electrode were reported, which included Mn₃O₄, α -MnO₂ nanowires, Fe₂O₃, Fe₃O₄, CuO and CoFe₂O₄, nano MnO_x powder, Pt particles, Pd/MnO₂ composite, carbon supported MnO_x, Pt-Au nanoparticles, CoMn₂O₄ spinel/graphene composite, graphene, etc. Graphene, which is a two dimensional planar sheet of sp² bonded carbon atoms, has attracted considerable interest in electrochemical applications. Graphene has high electronic

conductivity, large surface area and high electron-transfer rates. It has been studied for applications in fuel cells, electrical double-layer capacitors, Li-ion batteries and also for Li-air cells as described above. Au-based catalysts were studied as catalysts for bi-functional oxygen electrode reaction. Nanoparticles of PtAu were synthesized by reducing HAuCl_4 and H_2PtCl_6 by oleylamine and then loaded on Vulcan carbon to get 40 wt% PtAu/C. A discharge capacity of about 1500 mAh g^{-1} was obtained from Li- O_2 cells using this catalyst for O_2 electrode. In another study, nanoporous Au film was prepared by dealloying white gold leaf by treatment in concentrated HNO_3 . A free standing porous Au film was used as a catalyst for O_2 electrode. A reversible capacity of 325 mAh g^{-1} for Li- O_2 cells was reported.

As it is evident from a study of the above reports, development of an appropriate catalyst for O_2 -electrode reaction is an important aspect in the progress of research on rechargeable Li- O_2 cells. High discharge capacity, high values of coulombic and energy efficiency and long cycle-life are the key issues. It is attempted to address these issue by combining the favorable properties of graphene and silver, gold and iridium nanoparticles in the present study. Composites of metal nanoparticles anchored to reduced graphene oxide (RGO) are prepared and studied as the catalyst for reversible O_2 electrode of Li- O_2 cells. In the *in situ* synthesis procedure, the adsorbed metal ions on graphene oxide (GO) are reduced, which results in the formation of well dispersed nanoparticles of anchored to RGO layers. The Ag-RGO, Au-RGO, Pd-RGO, Ir-RGO and also PPY-RGO (PPY: polypyrrole) catalysts exhibit high catalytic activity for bi-functional reduction and oxidation kinetics of O_2 electrode. High discharge capacity and moderate charge-discharge cycling stability are reported.

2. EXPERIMENTAL DETAILS

2.1. Synthesis of Ag-RGO, Au-RGO, Pd-RGO, Ir-RGO, and PPy-RGO

For the preparation of Ag-RGO, graphite powder was first converted into graphite oxide (GtO) by the procedure described by Hummers and Hoffman. In brief, graphite powder (3.0 g) was added to 69 ml concentrated H_2SO_4 with 1.50 g NaNO_3 dissolved in it. The mixture was stirred for 1 h at ambient temperature. The container was cooled in an ice bath and 9.0 g KMnO_4 was added slowly while stirring the contents vigorously by a magnetic stirrer for about 15 min. The container was removed from the ice bath and allowed to warm up to ambient temperature. Two aliquots of 138 ml and 420 ml double-distilled water were added slowly and carefully in about 15 min intervals. Subsequently, 7.5 ml 30% H_2O_2 was added and the colour of the suspension changed from light yellow to brown, indicating the oxidation of graphite to GtO. The product GtO was separated by centrifugation washed with warm water and ethanol several times and dried at 50°C for 12 h. GtO (400 mg) was transferred into 800 ml double-distilled water and sonicated for 3 h. GtO was exfoliated to graphene oxide (GO) by sonication, which was separated by centrifugation, washed with double-distilled water and ethanol followed by drying at 50°C for 12 h. AgNO_3 (157 mg) was added to 100 mg GO was dispersed in 600 ml double-distilled water, sonicated for 30 min, then 1 M KOH (100 ml) was added slowly while stirring the contents. Finally, 1 M ethylene glycol (100 ml) was added as a reducing agent and the container was kept at 80°C for 3 h while stirring the contents. The product, Ag-RGO was separated by centrifugation, washed copiously with double-distilled water and ethanol, and dried at 60°C for 12 h. The quantities of AgNO_3 (157 mg) and GO (100 mg) were taken for the formation of Ag-RGO with mass ratio of Ag:RGO at 1:1. The product Ag-RGO was analysed for the quantity of

Ag by inductively coupled plasma emission spectroscopy and the quantity Ag present in Ag:RGO was 47 wt%, which closely agrees with the theoretical value (50 wt%). RGO was also prepared in a similar procedure in the absence of AgNO_3 .

For the preparation of Au-RGO, 0.154 g AuCl_3 was dissolved in 100 ml double-distilled water and 100 mg GtO was added. The contents were sonicated for 15 min, and then 100 ml Na_2CO_3 solution (5 wt%) was added drop-wise while stirring the contents. 1.20 g NaBH_4 was added to reduce both GtO and Au^{3+} simultaneously while stirring the contents by a magnetic stirrer. The contents were kept at 80°C and stirred for 1 h. The product of Au decorated RGO was separated by centrifugation, washed with double distilled water and ethanol, and dried at 60°C for 12 h. The mass ratio of Au and RGO was 1:1. The preparation method of Pd-RGO and Ir-RGO is same as of Au-RGO. For the preparation of Pd and Ir metal nanoparticles AuCl_3 is replaced by PdCl_2 and IrCl_3 . In all the cases the mass ratio of metal particles/RGO ratio was maintained at 1:1.

For the preparation of RGO-PPY composite, 1 ml pyrrole (Aldrich) was dissolved in 10 ml 0.1 M HCl and 100 mg RGO was added. The mixture was stirred for 12 h at ambient conditions and cooled to $< 4^\circ\text{C}$ in an ice bath. Ammonium persulphate (3.6 g) was dissolved in 0.1 M HCl, cooled to $< 4^\circ\text{C}$, and then added drop-wise to the suspension consisting of RGO and pyrrole. The contents were stirred for 6 h to facilitate the oxidation of pyrrole to PPY. The RGO-PPY (weight ratio 1:1) composite was separated by centrifugation, washed repeatedly with water and finally with ethanol. It was dried at 50°C .

2.2. Electrode preparation for rotating disk electrode (RDE) studies

For the electrochemical characterization studies by rotating disc electrode (RDE), 1.8 mg Ag-RGO and 4 μ l Nafion (5 wt% solution) were dispersed in 2 ml ethanol by sonication for 30 min. The suspension (200 μ l) was dropped on a glassy carbon (GC) disk electrode of area 0.07 cm^2 (diameter: 3mm) and solvent was evaporated in air. The quantity of Ag–RGO composite was 200 μ g on the GC electrode (2.8 mg cm^{-2}).

2.3. Oxygen electrode preparation and cell assembly

For the preparation of O_2 electrodes for Li- O_2 cells, porous carbon paper (Toray) of 2.0 mm thickness was used as the current collector. One side of the carbon paper was coated with carbon diffusion layer and the other side with the catalyst layer. A circular (12 mm diameter) disk was punched out of a sheet of Toray carbon paper. High surface area ($1500 \text{ cm}^2 \text{ g}^{-1}$) carbon powder (Fuzhou Yihuan Carbon, Co., China) and PTFE suspension (Aldrich) were mixed in 70:30 weight ratio. A minimum quantity of water was added to form dough, which was rolled into a layer. This layer (180 mg cm^{-2}) was applied on one side of the carbon paper current collector. The Ag-RGO catalyst and PVDF were mixed (weight ratio: 92.5:7.5) in a mortar, a few drops of NMP were added to form an ink. The ink was coated on the other side of the carbon paper. The mass of catalyst was 1 mg cm^{-2} . The sandwich of diffusion-layer, carbon paper and catalyst-layer was pressed in a die at a pressure of 50 kN for 3 min. The electrode was dried at 100°C for 12 h and transferred into an argon filled MBraun glove box model Unilab. Li- O_2 cells were assembled in home-made Swagelok-type PTFE containers. The container had provision to close on one side where Li disk anode was placed and the other side open for exposure to oxygen gas from a cylinder. A Li disk used as the anode (12 mm diameter) was punched out of a ribbon

(0.3mm thick) and its surface was scraped with a knife to remove a surface layer on both sides of it. Stainless steel current collectors were used to take electrical contacts from the electrodes. The Li disk, a glass mat separator and the air electrode were sandwiched inside the PTFE container and stainless steel electric contacts were inserted and sealed. The glass mat was soaked in the electrolyte, which was made of 1.0 M LiPF_6 in DMSO, before inserting into the cell. The catalyst-layer of the O_2 electrode was exposed to the electrolyte and the diffusion-layer to oxygen gas. The electrode preparation (O_2 electrode) for other catalyst is similar to Ag-RGO.

2.4. Characterization studies

For sonication during different stages of preparation of RGO and Ag-RGO, a Misonix ultra sonicator model S4000-010 was used. It was operated with a frequency of 20 kHz and power output of 600W. Titanium horn (diameter = 12 mm) was dipped in the aqueous phase and sonicated for the required duration. A Remi ultracentrifuge model R-8C was used to separate the solid samples from liquid phase. Powder X-ray diffraction patterns were recorded using a Philips 'X'PERT PRO diffractometer with Cu-K_α radiation (λ : 1.5438 Å) as the X-ray source. UV-visible spectra were recorded by Perkin-Elmer Lambda 35 UV-visible spectrometer. For this purpose, samples were prepared by sonication in double-distilled water for about 10 min and transferred into a quartz cuvette. FT-IR spectra of powder samples were recorded in a 1000 Perkin Elmer FT-IR spectrometer. Microscopy of the samples was carried out using FEI Tecnai T-20 200 kV transmission electron microscope (TEM). Atomic force microscopy (AFM) experiments were recorded using Digital Instrument Veeco Multimode AFM. Rotating disk electrode experiments were conducted using Autolab RDE setup and Autolab potentiostat/galvanostat model PGSTAT 30. The rotation speed of RDE was varied in a wide

range from 100 to 3000 rpm while sweeping the potential at 10 mV s^{-1} in ORR range. The reference electrodes used include saturated calomel (SCE) in the neutral electrolyte, Hg/HgO, 1 M KOH (MMO) in the alkaline electrolyte and a Pt wire pseudo reference electrode in the non-aqueous electrolyte. All potential values are converted into standard hydrogen electrode (SHE) scale and are presented. Charge-discharge cycling of Li-O₂ cells was carried out by using Bitrode battery cycling equipment in an air-conditioned room at $22 \pm 1^\circ\text{C}$.

3. RESULTS AND DISCUSSION

3.1. XRD studies

Formation of RGO and Ag-RGO from graphite powder was examined by powder XRD studies. The patterns of graphite, GtO, GO, RGO and Ag-RGO are shown in Fig. 1. Graphite (Fig.1a curve i) is characterized by the strong (002) reflection at 26.5° , corresponding to hexagonal graphitic structure. The inter-layer distance of (002) reflection obtained for graphite is 3.38 \AA . This value is comparable with the reported values. In the pattern of GtO, the (002) reflection is shifted to 10.3° (Fig.1a curve ii).

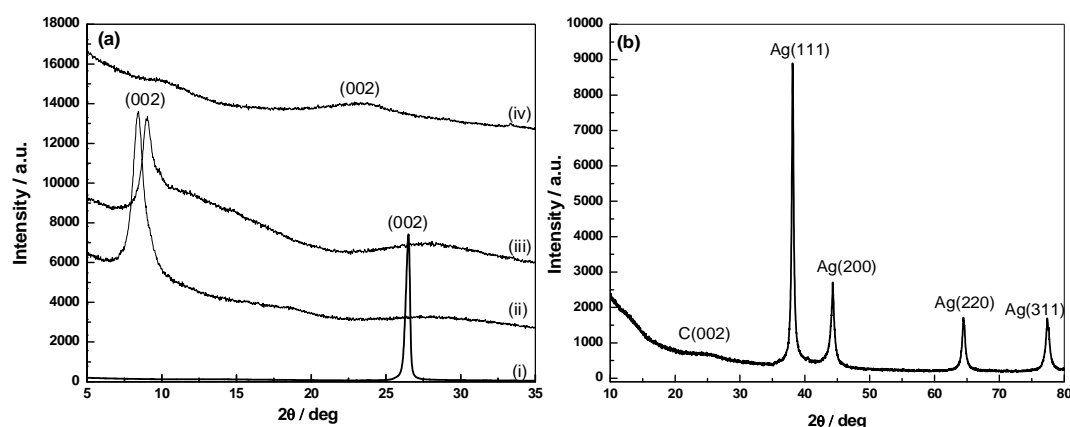


Fig. 1. Powder XRD patterns of (a) graphite (i), graphite oxide (GtO) (ii), graphene oxide (GO) (iii), reduced graphene oxide (RGO) (iv), and (b) Ag-RGO.

This value corresponds to an inter-layer distance of 8.48 Å, indicating expansion of graphite due to the presence of oxygen containing functional groups on both sides of graphene sheets and also atomic scale roughness due to sp^3 bonding in carbon. There is a shift in the (002) reflection of

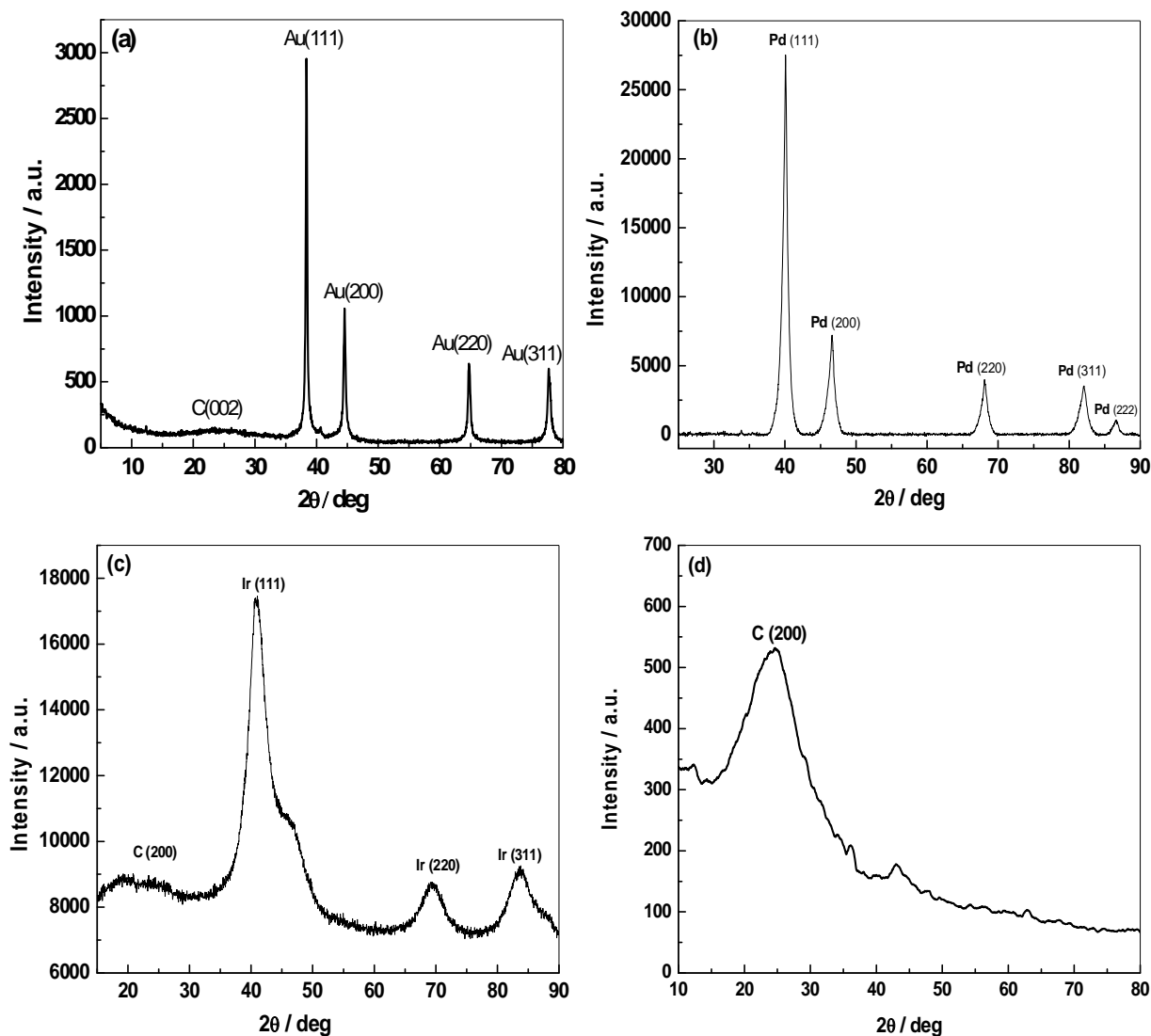


Fig. 2. Powder XRD patterns of (a) Au-RGO, (b) Pd-RGO, (c) Ir-RGO and (d) PPY-RGO.

GO (Fig. 1a curve iii) indicating the conversion of GtO to GO. RGO is characterized by the low intensity, broad (002) reflection (Fig. 1a curve iv). It is known that the diffraction peaks become weak or even disappear when regular stacking of GO is disturbed. The broad, weak (002) reflection is also attributed to small sheet size ($\leq 1 \mu\text{m}$) and a short domain order or turbostratic arrangement of RGO stacked sheets. The XRD pattern of Ag-RGO (Fig. 1b) consists of a broad reflection at 24.2° corresponding to the (002) plane of RGO and strong reflections at 38.1 , 44.3 , 64.4 and 77.4° , which are assigned to (111), (200), (220) and (311) planes, respectively, of face-centered cubic structure of Ag (JCPDS file 04-0783). Thus, XRD studies (Fig. 1a and b) suggest the conversion of graphite powder to RGO and Ag-RGO via formation of intermediates of GtO and GO. The strong reflections at $2\theta=38.2$, 44.5 , 64.5 and 77.9° , which are assigned to (111), (200), (220) and (311) planes, respectively, of face-centered cubic crystals of Au (JCPDS file 04-0783) (Fig 2a). The crystallite size calculated from Au(111) reflection using Scherrer's formula is 24.7 nm . The XRD pattern of Pd-RGO (Fig. 2b) consists of strong reflections at 40.0 , 46.5 , 68.2 , 82.0 and 86.5° , which are assigned to (111), (200), (220), (311) and (222) planes, respectively, of fcc Pd (JCPDS 04-0783). The XRD pattern of Ir-RGO (Fig. 2c) consists of strong reflections at 40.7 , 69.4 and 83.8° , which are assigned to (111), (220) and (311) planes, respectively, of face-centered cubic structure of Ir (JCPDS file 65-1686). Thus XRD studies suggest the conversion of graphite powder to RGO, Au-RGO, Pd-RGO and Ir-RGO. The XRD of RGO-PPY composite has a low intensity reflection at 24.30° , which is broader than the reflection of RGO in the absence of PPY (Fig. 2d). This feature supports the presence of PPY on graphene sheets

3.2. UV and IR spectroscopy

UV-visible spectra of GO, RGO and Ag-RGO are presented in Fig. 3a. The 245 nm band of GO (Fig. 3a curve i) is a characteristic feature of π - π^* transition of aromatic C-C bond and the shoulder at 307 nm is attributed to n - π^* transition of C=O bond. The spectrum of RGO (Fig. 3a curve ii) is characterized by 262 nm band, which is red shifted from 245 nm of GO. The absence of 307 nm shoulder indicates reduction of GO to RGO. In the spectrum of Ag-RGO (Fig. 3a curve iii), a new band at 410 nm appears which is attributed to electronic interaction of Ag nanoparticles with graphene sheets. IR-spectra of GO and Ag-RGO are shown in Fig. 3b. The band at 3620 cm^{-1} present in the spectrum of GO (Fig. 3b curve i) is attributed to stretching of O-H bond on the GO surface. The bands at 1709 , 1584 , 1222 and 1039 cm^{-1} are assigned to C=O, C=C, C-OH and C-O stretching vibrations, respectively. In the spectrum of Ag-RGO (Fig. 3b curve ii), the absorption bands at 3620 cm^{-1} (O-H bond) and 1709 cm^{-1} (C=O bond) are absent suggesting the reduction of GO to RGO. The UV and IR spectra of Au-RGO, Pd-RGO and Ir-RGO are similar to the spectrum of Ag-RGO.

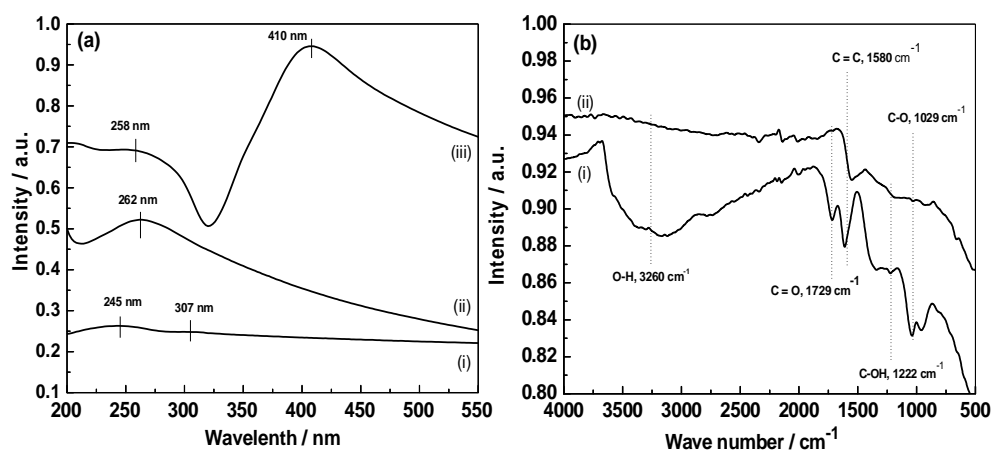


Fig. 3 (a) UV spectra of graphene oxide (i), RGO (ii), and Ag-RGO (iii), and (b) IR spectra of graphene oxide (i) and Ag-RGO (ii).

3.3. Atomic force microscopy studies

Atomic force microscopy (AFM) data of RGO and Ag-RGO are presented in Fig. 4. The thickness values of RGO are about 2 and 5 nm, respectively, in bare RGO and Ag-RGO composite (Fig. 4a and b). Different values of thickness ranging from 0.35 to 1.0 nm are reported for single graphene layer. It is thus inferred that the RGO and Ag-RGO prepared in the present study consists of a few layers of graphene. AFM images of Au-RGO, Pd-RGO and Ir-RGO are similar to Ag-RGO.

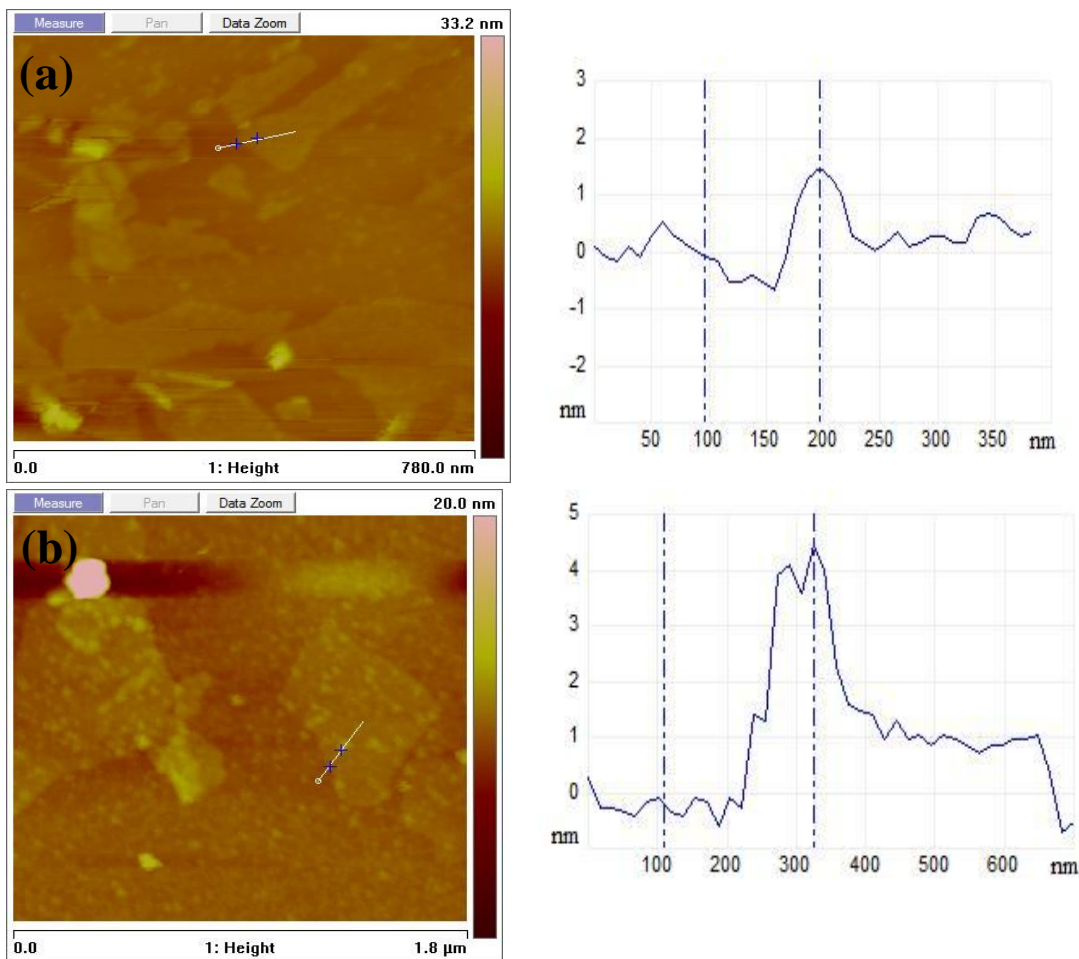


Fig. 4. AFM images of (a) RGO and (b) Ag-RGO composite.

3.4. X-ray photoelectron spectroscopy

The survey of the XPS spectra of Ag-RGO shows the presence of the element like Ag, C, O (Fig. 5a). XPS spectrum of Ag-RGO corresponding to 3d core level of Ag (Fig 5b) consists of a doublet at 368.3 and 374.3 eV. The separation of $3d_{5/2}$ and $3d_{3/2}$ by 6.0 eV indicates the metallic nature of Ag on RGO sheets.

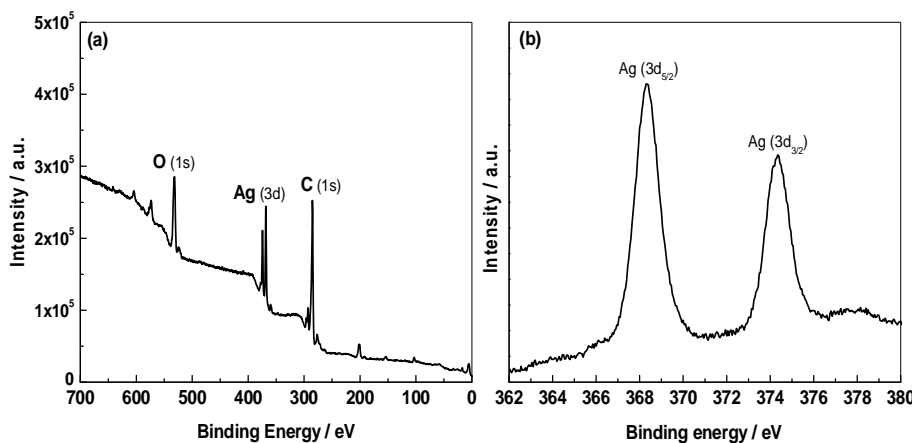


Fig. 5. XPS spectra of (a) Ag-RGO and (b) Ag 3d region.

The presence of Au in Au-RGO and Ir in Ir-RGO was also examined by recording XPS spectrum (Fig. 6). In the survey spectrum, signals corresponding to Au (4p, 4d and 4f regions) Ir (4p, 4d and 4f regions) as well as C 1s region are present (Fig. 6). The deconvoluted spectrum of C 1s (Fig. 6b), it shows the presence of C-C, C-O, and C=O bonds at 284.6, 286.5 and 288.1 eV, respectively. It is known that small quantity of O is present in RGO obtained by the reduction of graphene oxide (Fig. 6b). The Au 4f region is split into $4f_{7/2}$ and $4f_{5/2}$ peaks at 83.9 and 87.5 eV (Fig. 6c). The peak separation of 3.6 eV for Au 4f doublet indicates metallic nature of Au on RGO. The deconvoluted spectrum of Pd-RGO corresponding to 3d core level of Pd (Fig. 6d)

consists of a doublet at 33.5 and 341 eV. Deconvoluted XPS spectrum of Ir-RGO corresponding to 4f core level of Ir (Fig. 6e) consists of a doublet at 61.4 and 64.4 eV. Surface oxidation of Ir results in the formation of IrO₂ as a minor component.

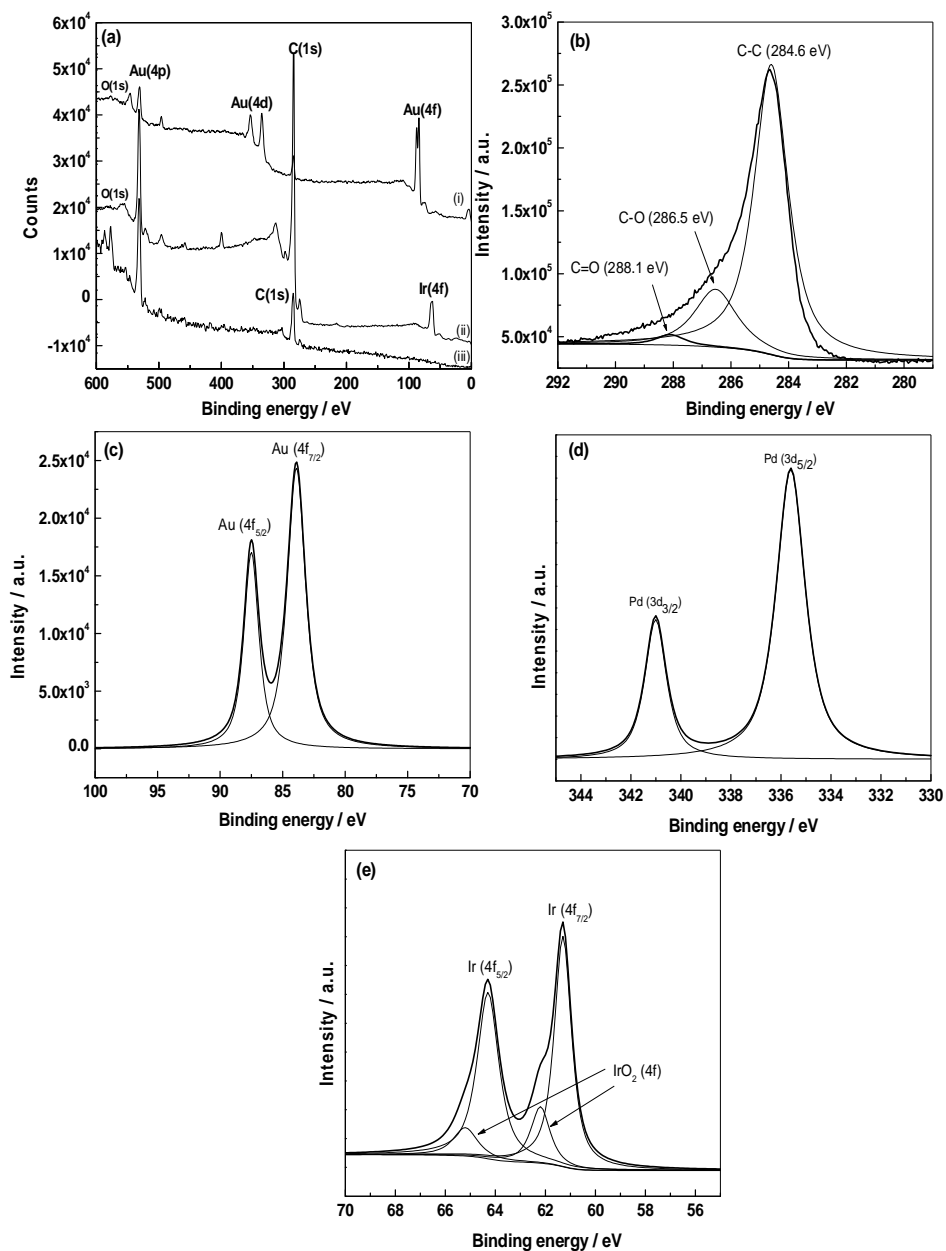


Fig. 6. (a) Survey of XPS spectra of (i) Au-RGO, (ii) Ir-RGO and (iii) carbon, and deconvoluted spectra of (b) C 1s, (c) Au 4f, (d) Pd 3d and (e) Ir 4f orbitals.

3.5. Raman spectroscopy

Raman spectra of RGO, Au-RGO and Ir-RGO are shown in Fig. 7a. The two bands at about 1358 cm^{-1} and 1522 cm^{-1} are assigned to the disorder induced D-band and in-phase vibration of the graphene lattice (G-band), respectively. The D-band originates from defects of graphene and it is absent in Raman spectra of defect-free samples. The G-band corresponds to the E_{2g} mode, which results from the vibration of sp^2 bonded carbon atoms. In a literature report, when Au, Ag, Ir, Pt and Pd-nanoparticles were deposited on graphene, the intensity of the D-band increased relative to the G-band and both D and G-bands shifted to higher wave numbers. A relationship between ionization energy of the metal and shift in the position of G-band was proposed. The magnitude of the G-band shift decreased with an increase in ionization energy of the metal. From these features of Raman spectra, the presence of electronic interaction between the metal particles and graphene was inferred. In the present study, the intensity ratio of D and G bands for RGO (Fig. 7a curve i) is 0.93, whereas this ratio for Au-RGO (Fig. 7a curve ii) is 1.08, and Ir-RGO (Fig. 7a curve iii) is 1.00. Furthermore, there is a shift of G-band from 1595.3 cm^{-1} in RGO to 1599.7 cm^{-1} in Au-RGO. Thus, the shift in G-band is 4.4 cm^{-1} in the present study, whereas a shift of 2.0 cm^{-1} was reported for Au-graphene. These results suggest the existence of electronic interaction between Au and RGO in Au-RGO. The RGO spectrum shows intense bands at 1588 and 1350 cm^{-1} , which are known as G and D bands of graphene sheets arising from in plane vibration of graphite lattice (E_{2g}) and the defect sites of smaller graphene domains, respectively. In addition to these bands, the spectrum of RGO-PPY also contains less intense bands at 639 , 933 , 973 and 1048 cm^{-1} . The bands near 1588 and 1350 cm^{-1} of PPY-RGO are also attributed the π -conjugated structure and ring stretching mode of PPY backbone, respectively. The band at 1048 cm^{-1} is due to the C-H in plane deformation arising from pyrrole ring, and the

bands at 973 and 933 cm^{-1} are associated with the quinoid polaronic and bipolaronic structure, respectively. The ratio of intensities of D and G bands (I_D/I_G) of RGO-PPY is 0.85, whereas it is 1.13 for RGO. This indicates RGO sheets are more ordered in RGO-PPY composite, probably due to electronic interactions from PPY.

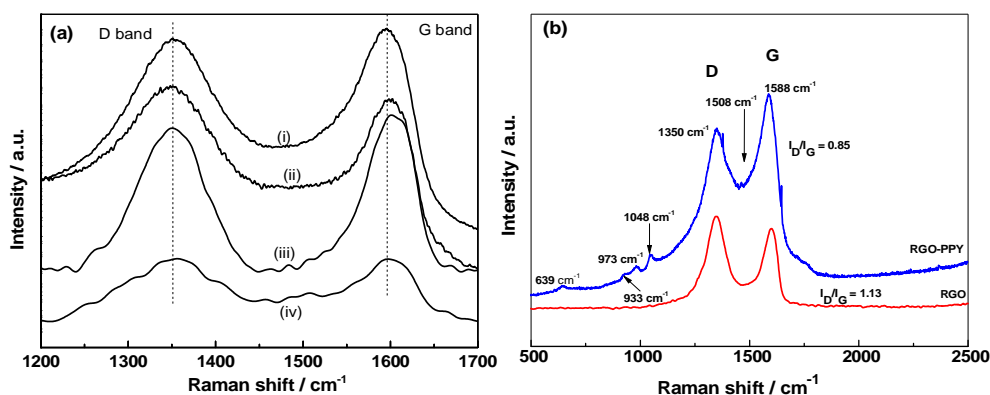


Fig. 7. Raman spectra of (a) RGO (i), Au-RGO (ii), Pd-RGO (iii) and Ir-RGO (iv), and (b) PPY-RGO.

3.6. Microscopy

Scanning microscopy (SEM) images (Fig. 8a and b) indicate a layer-like morphology in both RGO and Ag-RGO samples. Tunneling microscopy (TEM) images, particle size distribution and electron diffraction pattern of Ag-RGO sample are presented in Fig. 8c-f. The TEM images (Fig. 8c and d) reveal the presence of layers of RGO and nanoparticles of Ag distributed uniformly on them. Particle size distribution plot (Fig. 8e) suggests the presence of Ag particles in 2-7 nm range with an average size of 4.7 nm. The preparation of Ag-RGO involves simultaneous reduction of Ag^+ ions and GO

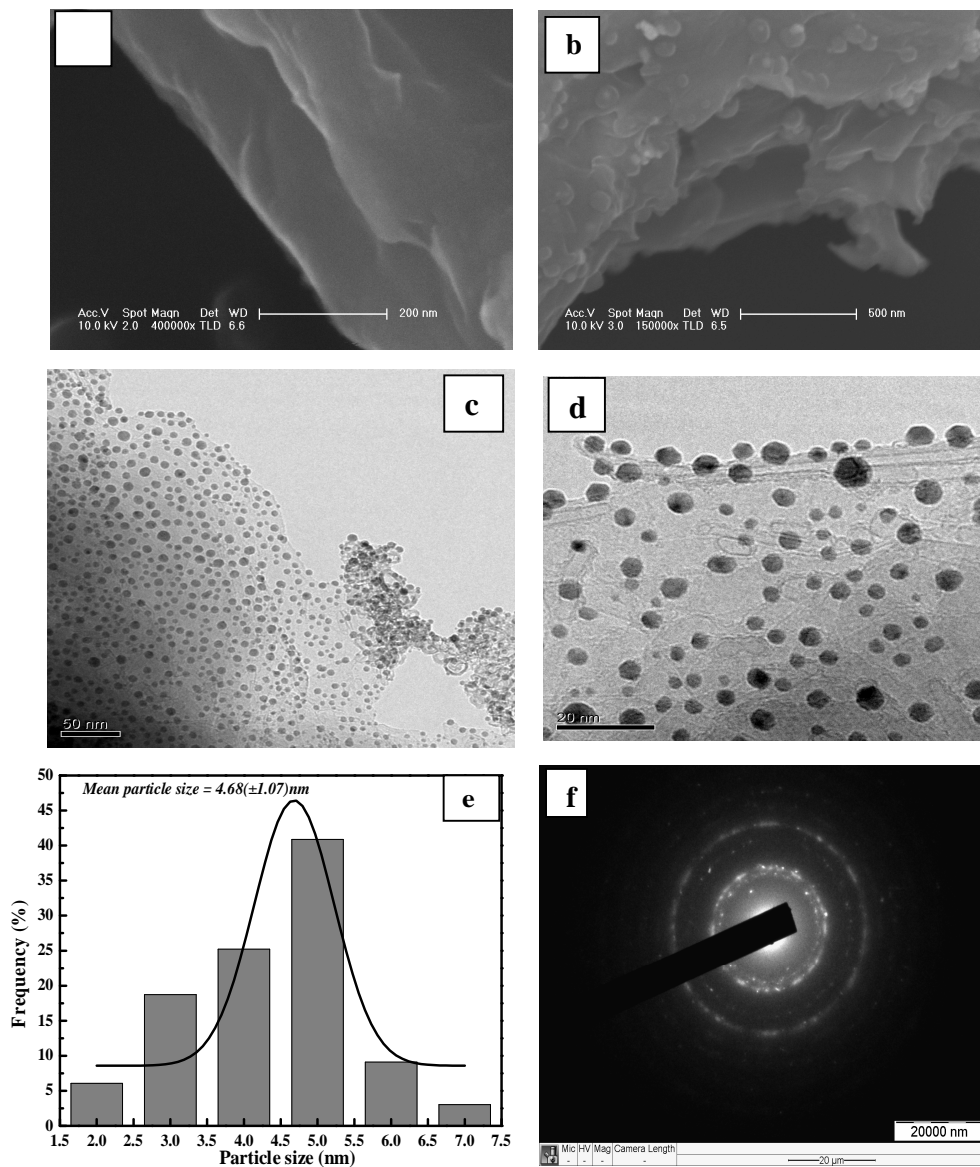


Fig. 8. SEM images of RGO (a) and Ag-RGO (b), TEM images of Ag-RGO in different magnifications (c, d), particle size distribution of Ag-RGO (e) and diffraction pattern of Ag-RGO (f).

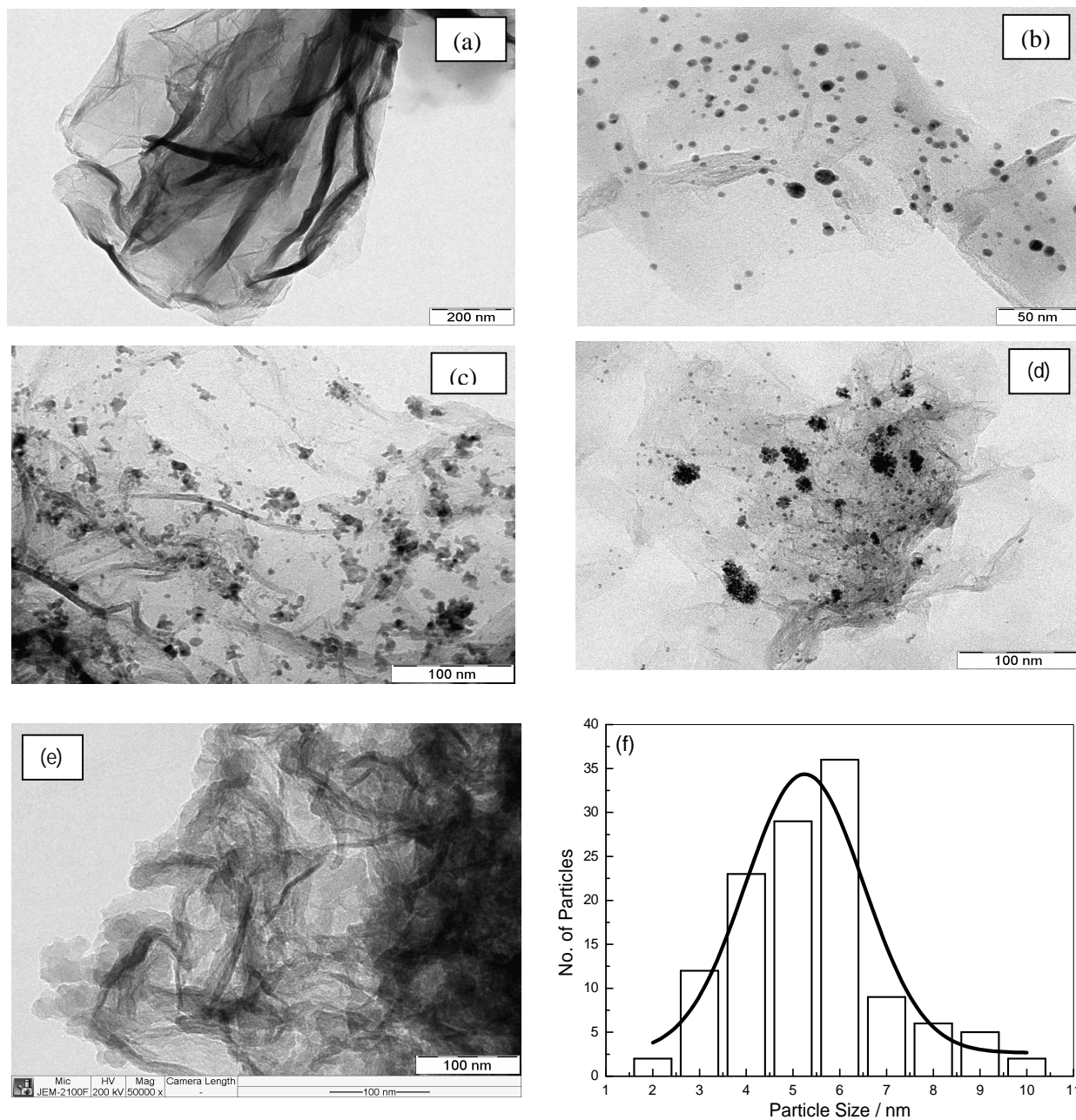


Fig. 9. TEM image of (a) RGO, (b) Au-RGO, (c) Pd-RGO, (d) Ir-RGO and (e) PPY-RGO; and (f) particles size distribution of Au

present in the reaction medium by ethylene glycol. It is interesting to note that Ag nanoparticles are anchored uniformly over the sheets of RGO, instead of existing as a separate phase. It is thus inferred that Ag^+ ions are adsorbed on the surface of GO sheets, which possess interlayer separation of 8.48 Å. This is due to the presence of oxygen species on GO surface and their chemical interaction with Ag^+ ions. Subsequent to the addition of ethylene glycol, GO as well as the adsorbed Ag^+ ions undergo simultaneous reduction, thus, producing Ag anchored RGO layers. Electron diffraction pattern (Fig. 8f) indicates polycrystalline nature of Ag nanoparticles.

TEM images of Au-RGO, Pd-RGO, Ir-RGO, and PPY-RGO sample are presented in Fig. 9. Layers of graphene are clearly seen in TEM image of pure graphene without metal nanoparticles (Fig. 9a). The TEM images (Fig. 9 b-e) reveal that nanoparticles of Au, Pd and Ir are distributed uniformly on graphene sheets. The preparation of metal particle-RGO involves simultaneous reduction of the metal ions and GO present in the reaction medium by NaBH_4 . It is interesting to note that nanoparticles and RGO are not present as separate constituents. But they are anchored uniformly over the sheets of RGO. It is thus inferred that Au^{3+} , Pd^{2+} and Ir^{3+} ions are adsorbed on the surface of GO sheets, which possess inter-layer separation of 8.48 Å, before undergoing reduction. This is due to the presence of oxygen species on GO surface and their chemical interaction with the metal ions. Subsequent to the addition of NaBH_4 , GO as well as the adsorbed ions undergo *in situ* reduction, thus, producing anchored metals particles RGO layers. TEM image of Ir-RGO shown in Fig. 9c. Ir particles have undergone agglomeration at a few spots. Particle size distribution measured from non-agglomerated particles and it indicates the presence of Ir nanoparticles in the sizes 3-10 nm, with an average size of 3.9 nm. The distribution of Ir indicates that Ir^{3+} interact with oxygen functionalities in GO. When GO and Ir^{3+} ions are subjected to simultaneous reduction, the interaction facilitates Ir metal nanoparticles to

anchor on the surface of RGO sheets. In the TEM image of RGO-PPY (Fig. 9e), the formation of uniform layer of PPY on RGO is observed.

3.7. Electrochemical studies on Ag-RGO in KOH electrolyte

3.7.1. Cyclic voltammetry

Cyclic voltammogram of GO, RGO and Ag-RGO coated GC electrodes indicate that the reduction of O_2 does not take place at GO in 1M KOH electrolytes (Fig. 10a). There is a reduction current peak at -0.06 V in the voltammogram of both RGO and Ag-RGO. However, the peak current of Ag-RGO is greater than that of RGO.

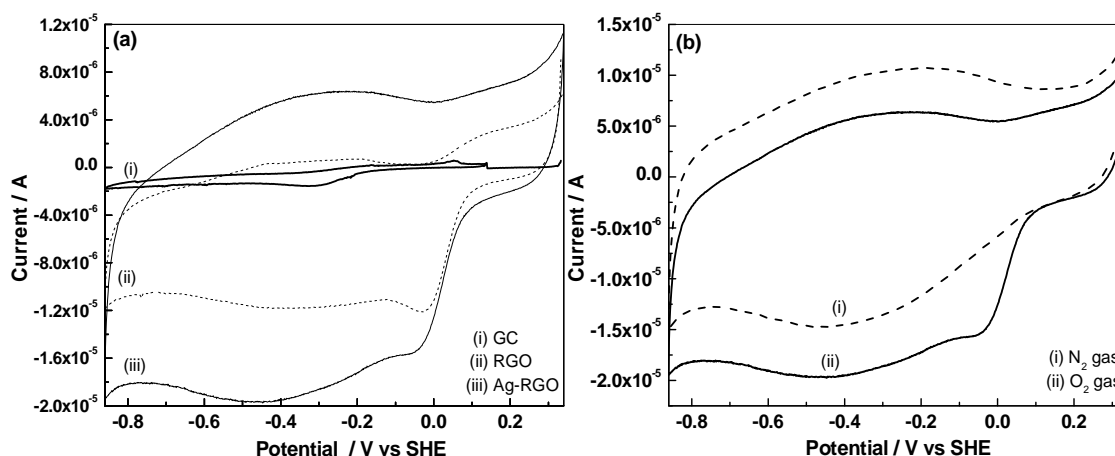


Fig. 10. Cyclic voltammograms of (a) ORR on GC, RGO and Ag-RGO, and (b) after saturation with N_2 and O_2 gas in 1 M KOH electrolyte at 10 mV s^{-1} .

Voltammograms of Ag-RGO coated GC electrode were recorded in O_2 saturated as well as N_2 saturated KOH electrolyte (Fig. 10b). When scanned from 0.24 V to -0.04 V, there was a reduction current peak at -0.06 V in O_2 saturated 1M KOH electrolyte. By repeating the

experiment after saturating with N₂ gas, the reduction peaks disappear. Several repetitions were carried out by passing O₂ and N₂ gases alternately, and ensured that the reduction peak appearing at -0.06 V originated from O₂ (Fig. 10b). Thus the current peak was attributed to the reduction of O₂ (Reaction 1) catalyzed by Ag nanoparticles dispersed on RGO.



The voltammograms of Ag-RGO were broad (Fig. 10b) without sharp current peak corresponding to reaction (5). This was likely to be due to capacitance behaviour of RGO, which was due to adsorption of ions from the electrolyte. Experiments were repeated at several sweep rates (v), and dependence of peak current density (i_p) on sweep rate was examined. A linearity of i_p versus $v^{1/2}$ plot indicated diffusion controlled reduction of ORR on Ag-RGO electrode. Thus it was concluded that Ag nanoparticles dispersed on RGO catalysed ORR.

3.7.2. Rotating disk electrode studies

Linear sweep voltammograms of Ag-RGO coated GC were recorded at a sweep rate of 10 mV s⁻¹ with different speeds of RDE in 1M KOH solution saturated with O₂ (Fig. 11a). At all speeds of RDE, current is negligibly small between 0.24 and -0.04 V. Reduction current starts increasing at 0.04 V and at it is nearly steady between -0.11 and -0.86 V. Current between 0.40 to -0.11 V is due to mixed control by both electron transfer and diffusion. The steady-state current is due to diffusion controlled ORR (Reaction 1). The diffusion-limited steady current density (i_L) is related to velocity of RDE ($\omega = 2\pi f$, f being the frequency in revolution per second) by Levich equation (eq. 5).

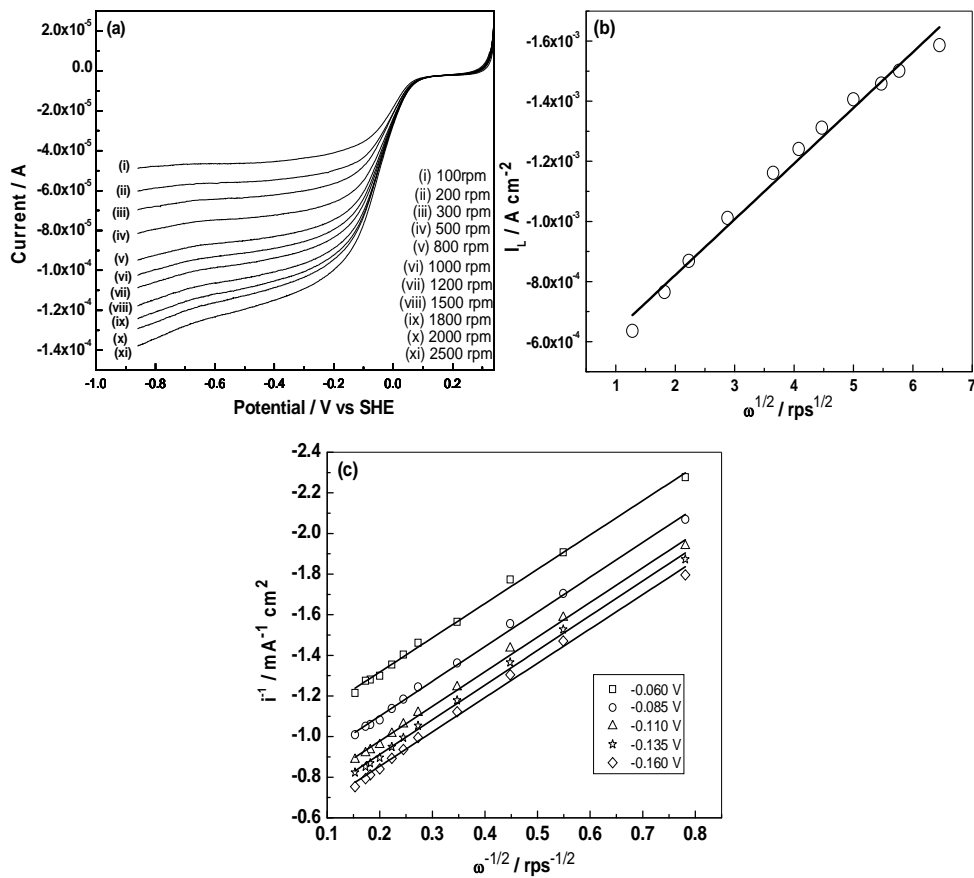


Fig. 11. (a) Linear sweep voltammetry of Ag-RGO for ORR at 10 mV s^{-1} after saturation with O_2 gas in different rotation speed range from 100 to 2500 rpm, (b) Levich plot, and (c) Koutecky-Levich plot.

$$i_L = 0.62 n F D^{2/3} \eta^{-1/6} c^o \omega^{1/2} \quad (6)$$

where D is diffusion coefficient of dissolved O_2 , η is kinematic viscosity of solution, c^o is concentration of O_2 in electrolyte and other symbols have their usual definitions. The data presented in Fig. 11b suggest that the limiting current is a steady value between -0.26 and -0.86 V at low rpm values of the RDE. A plot of i_L versus $\omega^{1/2}$ is presented in Fig. 11b. The plot is linear suggesting the validity of Eq. (6).

In the limiting current region, current density depends on the rate of diffusion of O_2 across the stagnant layer as described above. This condition prevails in the potential range from -0.11 to

-0.86 V (Fig. 11c). However, at low current densities in the potential range 0.24 to -0.04 V, electron-transfer controls the rate of the ORR. In the intermediate range of potential (-0.04 to -0.16 V), the reaction is mixed control. In this region, Koutecky-Levich equation is valid.

$$\frac{1}{i} = \frac{1}{nFkc^0} + \frac{1.61 \eta^{1/6}}{nFc^0 D^{2/3}} \frac{1}{\omega^{1/2}} \quad (7)$$

where k is rate constant. A plot of i^{-1} versus $\omega^{-1/2}$ is expected to be linear. In Fig. 11c, i^{-1} versus $\omega^{-1/2}$ plots at different potentials in the range from -0.06 to -0.16 V are presented. The average value of D calculated from the slopes is $1.78 \times 10^{-5} \text{ cm}^2 \text{ s}^{-1}$, which agrees well with the value reported in the literature. The values of k obtained from the intercepts (Fig. 11c) are in the range 6.1 to $3.1 \text{ cm}^2 \text{ s}^{-1}$.

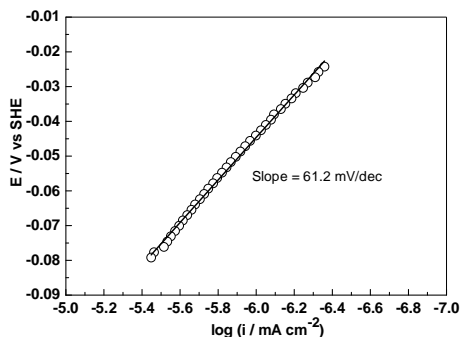


Fig. 12. Tafel plot of Ag-RGO for ORR in 1 M KOH.

In the electron-transfer controlled region, current-potential data were measured potentiostatically while stirring 1 M KOH solution, which was saturated with O_2 gas. The data are presented as Tafel plot in Fig. 12. The slope of Tafel plot is $61.2 \text{ mV decade}^{-1}$, which indicates that the rate determining step involves a 2-electron transfer in the potential regime of fast mass transport.

3.8. Electrochemical studies on Ag-RGO in non-aqueous electrolyte

3.8.1. Cyclic voltammetry

Kinetics of ORR was studied using cyclic voltammetry and RDE in acetonitrile consisting of different salt by Laoire et al. Although, a Li salt solution is required as the electrolyte for Li-air cell studies, such an electrolyte is found unsuitable for RDE studies employing a catalyst coated glassy carbon electrode. Formation of Li_2O and Li_2O_2 from the ORR deposit on the electrode surface leading to irreproducibility of experimental results. Therefore, TBAP dissolved in DMSO was used for CV and RDE studies in the present work. Cyclic

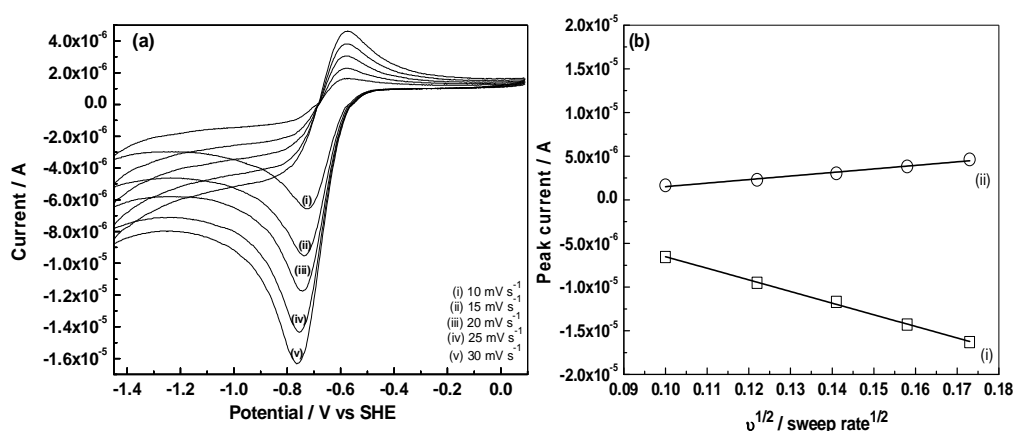


Fig. 13. (a) Cyclic Voltammetry of Ag-RGO for ORR activity at different scan rates and (b) plot between peaks current versus (sweep rate)^{1/2}.

voltammograms recorded at several sweep rates in 0.1 M TBAP-DMSO electrolyte at Ag-RGO coated GC electrode are shown in Fig. 13a. A cathodic current peak appears at -0.73 V in the forward sweep at 10 mV s⁻¹, which is attributed to the reduction of O_2 resulting in the formation of TBAO_2 .



The voltammograms shown in Fig. 13a are similar to those reported by Laoire et al., except that another pair of minor current peaks as reported in the literature is absent in Fig. 13a. The second minor cathodic peak was attributed to further reduction of TBAO₂ to TBA₂O₂ (reaction 5).



The cathodic current peak (P_c) in Fig. 13b is attributed to reduction of O₂ and the anodic peak (P_a) to the opposite reaction. As the anodic charge is less than the cathodic charge, it is inferred that oxygen reaction is partially reversible. The cathodic peak current density (i_{pc}) is considered to follow Randles-Sevcik equation (Eq. 6).

$$i_{pc} = (2.69 \times 10^5) n^{3/2} D^{1/2} \nu^{1/2} c^o \quad (10)$$

where n is number of electrons, D is diffusion coefficient of O₂, ν is sweep rate and c^o is concentration of O₂ in the electrolyte. A plot of i_{pc} versus ν^{1/2} is a straight line (Fig. 13b) indicating the ORR is controlled by diffusion of O₂. Similar observation is made for the anodic peak current density (i_{pa}) also from i_{pa} versus ν^{1/2} data (Fig. 13b). The two plots (Fig. 13b) have two different slopes due to differences in kinetics of ORR and OER.

3.8.2. Rotating disk electrode

Linear sweep voltammograms recorded in O₂ saturated 0.1 M TBAP-DMSO solution at several rotation speeds of RDE are presented in Fig. 14a. Similar to the data obtained in aqueous electrolytes discussed above, the voltammograms (Fig. 14a) are characterized by electron-transfer controlled regime at low potentials, diffusion-controlled regime with limiting current at

high potentials and a mixed regime in between. The low potential data were plotted as Tafel plot (Fig. 14d) and slope of 53 mV decade⁻¹ was obtained for the data recorded at 200 rpm. Similar

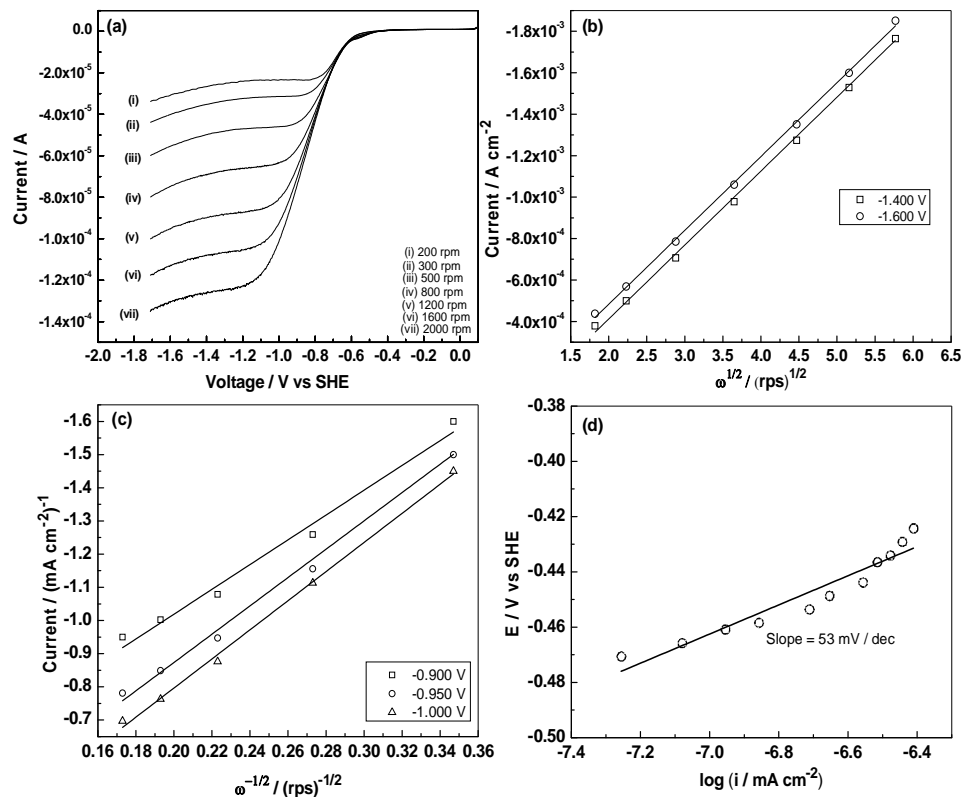


Fig. 14. (a) Linear sweep voltammetry of Ag-RGO for ORR at 10 mV s⁻¹ scan rate with different speed of rotation in 0.1M TBAP-DMSO, (b) Levich plot, (c) Koutecky-Levich plot, (d) Tafel plot for ORR.

values of slopes were obtained at higher rotation rates also. This value is close to 60 mV decade⁻¹ expected for a 2-electron transfer process. The diffusion controlled RDE data were analysed similar to the aqueous data and the values of D and n obtained are $1.62 \times 10^{-6} \text{ cm}^2 \text{ s}^{-1}$ and 0.7, respectively. The value of n close to unity indicates the formation of superoxide (O_2^-) in the non-aqueous electrolyte under diffusion-limited conditions.

3.9. Li-O₂ cell studies using Ag-RGO

The electrochemical properties of O₂ electrode of Li-O₂ cells in non-aqueous electrolytes depend on several factors including the properties of carbon, catalyst, nature of the current collector, method of electrodes fabrication and nature of the electrolyte. In the present work, 1.0 M LiPF₆ dissolved in DMSO is used as the electrolyte and porous Toray carbon paper is used as the current collecting substrate. On one side of the carbon paper, a diffusion-layer made of high surface area (1500 cm² g⁻¹) carbon powder with micropores of diameter less than 2 nm was coated at a loading level of 180 mg cm⁻². This side was exposed to O₂ gas. The other side of the carbon paper, which was exposed to the electrolyte, was coated with the catalyst. Several Li-O₂(Ag-RGO) cells were assembled and subjected to charge-discharge cycling with different currents. A few Li-O₂(RGO) cells without Ag catalyst were also assembled for comparison studies. Charge-discharge curves of Li-O₂(Ag-RGO) cells are presented in Fig. 15a for three different currents. The discharge capacity decreases with an increase in current as expected. At 0.2 mA cm⁻², the discharge plateau appears at about 2.50 V and the charge plateau at about 4.20 V. Thus, the difference in charge-discharge plateaus is about 1.70 V, which is a high value. For high reversible battery systems, the expected difference in charge-discharge plateaus is expected of the order of a few tens of mV. A large voltage gap is an inherent problem associated with Li-O₂ cells, which is observed, is several reports. With an increase in current density, there is an increase in voltage gap. Although the unit of capacity usually reported in the literature for Li-O₂ cell in mAh g⁻¹ on the basis of mass of catalyst loaded carbon, a more appropriate unit is mAh cm⁻². This is because of the fact that carbon or catalyst loaded carbon is not an active material, unlike a battery active material stored within the cell. In the latter case, the mass of electrode material generally stored in the cell is used for reporting specific capacity in mAh g⁻¹. In Li-O₂

cells, the mass of O_2 should be used in principle for calculation of specific capacity of O_2 electrode. Because O_2 is not stored inside in the cell, results are generally reported on the basis of mass of catalyst loaded carbon. The difficulty in using the mass of carbon arises because the loading level of carbon is varied over a wide range in the literature, and capacity is also known to decrease by increasing the mass of carbon. Therefore, the capacity values are additionally reported on the basis of electrode area in mAh cm^{-2} in the present work.

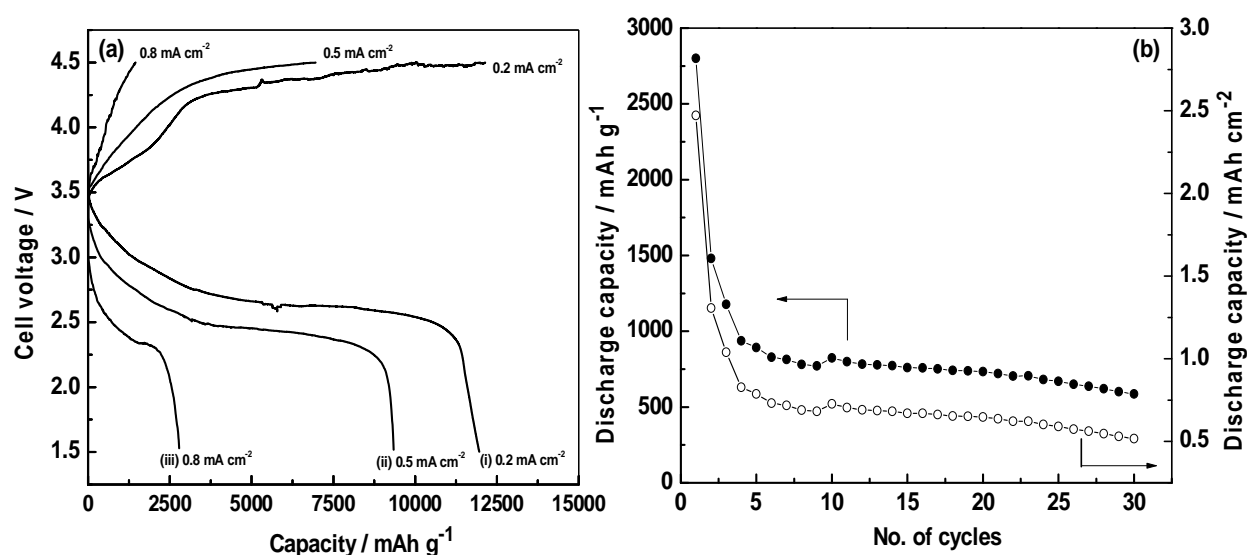


Fig. 15. (a) Charge - discharge curve of first cycle at different current densities, and (b) cycle life test at current density 0.8 mA cm^{-2} .

The discharge capacity values obtained are 11950 (11.29), 9340 (5) and 2780 mAh g^{-1} (2.47 mAh cm^{-2}), respectively, when discharged at 0.2, 0.5 and 0.8 mA cm^{-2} . It is interesting to note that the discharge capacity of 11950 mAh g^{-1} ($11.29 \text{ mAh cm}^{-2}$) obtained at 0.2 mA cm^{-2} is an extremely high value.

The charge-discharge reactions occurring at the electrodes are as follows.

At the negative electrode:



It is known that the reduction of O₂ in Li⁺ ion containing non-aqueous electrolytes results in the formation of Li₂O₂ and Li₂O as stable products during the discharge of Li-O₂ cell. Laoire et al., proposed the following mechanism for oxygen electrode reactions:



Single-electron transfer reduction of O₂ producing superoxide (O₂⁻) in non-aqueous electrolytes (reaction 12) is reported. Lithium superoxide undergoes another single-electron transfer reduction (reaction 13) forming lithium peroxide, which further undergoes two electron transfer reduction (reaction 14) forming the final reduction product, Li₂O. It is also reported that the reaction product is Li₂CO₃ in carbonate-based electrolyte. It is also believed that the reaction intermediate formed during oxygen reduction, namely, O₂⁻ is reactive towards most of the solvents used for the electrolyte, which may lead to the formation of Li₂CO₃. Li₂CO₃ cannot be oxidized back to O₂, thus affecting rechargeability and cycle-life of Li-O₂ cells. Alternate non-reactive solvents such as DMSO are suggested. The electrolyte used in the present study is 1.0M

LiPF₆ dissolved in DMSO. Lithium oxides are expected to be the major reaction products of oxygen reduction in the non-carbonate based electrolytes. In the present study also, Li₂O₂ and Li₂O are identified as the major products of O₂ reduction during the discharge of Li-O₂ (Ag-RGO) cells, as discussed later. During the charging process, Li₂O₂ and Li₂O are converted to O₂ following the reverse steps of reactions 10, 9 and 8 in sequence.

Li-O₂ (Ag-RGO) cells were tested for cycling stability at a current density of 0.8 mA cm⁻² over 30 cycles (Fig. 15b). Initially, about 2800 mAh g⁻¹ (2.47 mAh cm⁻²) is obtained. There is a rapid decrease in capacity to about 937 mAh g⁻¹ (0.82 mAh cm⁻²) at the 4th cycle. This is followed by a gradual decrease in capacity. About 586 mAh g⁻¹ (0.51 mAh cm⁻²) is obtained at the 30th cycle. When Li-O₂ (RGO) cells were cycled, the discharge capacity decreased rapidly in about 5-10 cycles and the cells could not be cycled thereafter. These results confirm the catalytic activity of Ag-RGO for oxygen electrode reaction in non-aqueous rechargeable Li-O₂ cells. Thus, Ag-RGO is a promising catalyst for rechargeable Li-O₂ cells

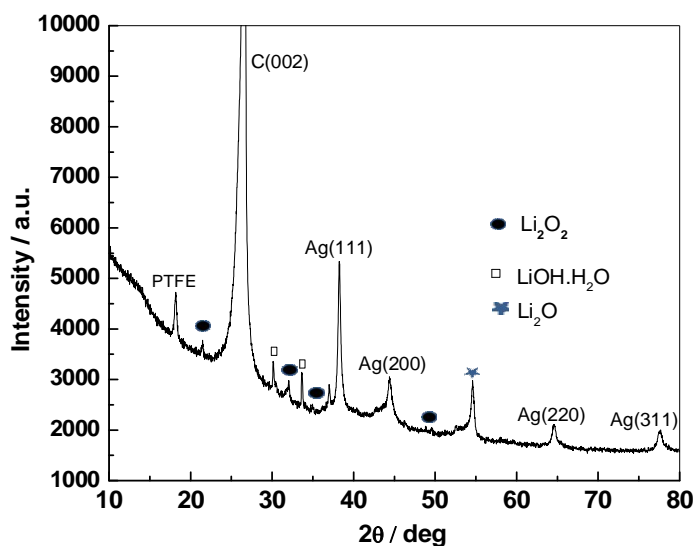


Fig. 16. XRD pattern of oxygen electrode of Li-O₂ cell after subjecting to five charge-discharge cycles.

In order to identify the reaction products of O_2 reduction on Ag-RGO in DMSO electrolyte, a few Li- O_2 (Ag-RGO) cells were assembled, subjected to five charge-discharge cycles and the cycling was terminated after the cells were discharged. The cells were disassembled, washed with acetone and XRD patterns of the oxygen electrodes were recorded (Fig. 16). The catalyst layers of a few used electrodes were scraped out of the carbon paper substrate and examined under TEM. The Ag nanoparticles are clearly observed on RGO of the used electrodes. There is an increase in particle size in comparison with fresh Ag-RGO. This may be due to mechanical stresses involved in the preparation of the electrodes and also in scraping of coating layers. The XRD patterns (Fig. 16) recorded for all electrodes were similar, thus, ensuring the reproducibility of the results. The (002) reflection of carbon is present at 26.4° . This is the most intense peak of the XRD pattern (Fig. 16) because of the presence of porous carbon paper current collector, diffusion layer made of carbon powder and also RGO present in Ag-RGO catalyst. The reflections corresponding to (111), (200), (220) and (311) planes of face-centered cubic crystal of Ag appear at 38.1 , 44.3 , 64.4 and 77.4° , respectively (Fig. 16). These reflections remain the same as those of the as prepared Ag-RGO catalyst (Fig. 1b). As there are no changes noticed in the crystal structure of Ag after repeated charge-discharge cycling, the stability of the catalyst is ensured. In addition to the reflections of carbon and Ag, there are a few more peaks or shoulders present in the cycled electrode. The reflection at 18.2° is attributed to the PTFE binder present in the electrode, the peak at 21.5 , 32.1 , 34.8 and 48.8° are due to Li_2O_2 , and a weak peak at 54.4° is due to Li_2O . Low intensity peaks present at 31.1 and 33.7° are attributed to $LiOH$ probably formed by hydrolysis of oxides of Li during handling of the electrodes in ambient atmosphere. Thus, Li_2O_2 and Li_2O are inferred as the products of O_2 reduction in the present study.

3.10. Electrochemistry of Au-RGO catalyst

3.10.1. ORR on Au-RGO in 1 M KOH electrolyte

Cyclic voltammograms of Au-RGO coated GC electrode were recorded in O_2 saturated as well as N_2 saturated KOH electrolyte (Fig 17a). When scanned from 0.0 V to -0.86 V, there was a reduction current peak at -0.31 V in O_2 saturated 1M KOH electrolyte. By repeating the experiment after saturating with N_2 gas, the reduction peak disappeared (Fig. 17a). Several repetitions were carried out by passing O_2 and N_2 gases alternately, and ensured that the reduction peak appearing at -0.31 V originated from O_2 . There is an increase in peak currents by increasing the sweep rate (Fig. 17b). Thus the current peak was attributed to the reduction of O_2 catalyzed by Au nanoparticles dispersed on RGO.

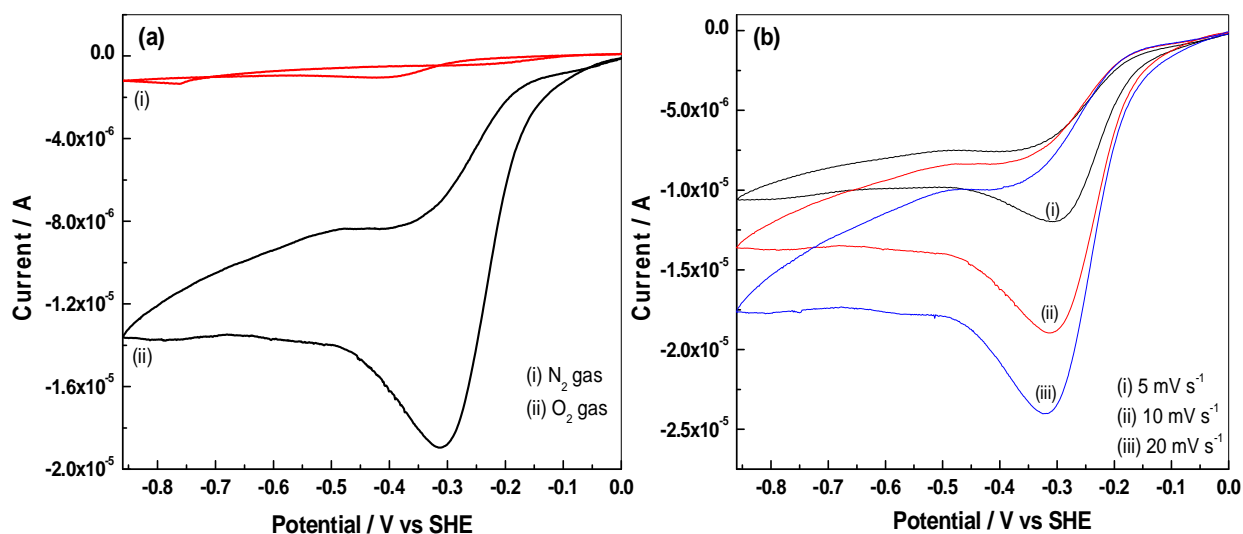


Fig. 17 (a) Cyclic voltammogram of Au-RGO coated GC electrode in 1 M KOH after saturation with N_2 and O_2 gases at the scan rate of 10 mV s^{-1} , and (b) after saturation with O_2 gas at different sweep rate.

Linear sweep voltammograms of Au-RGO coated GC were recorded at a sweep rate of 10 mV s^{-1} with different speeds of RDE in 1M KOH solution saturated with O_2 (Fig. 18a). At all speeds of RDE, current is negligibly small between -0.35 and -0.40 V. Reduction current starts increasing at -0.40 V and it is nearly steady between -0.47 and -0.6 V. Current between -0.35 to -0.47 V is due to mixed control by both electron transfer and diffusion. The steady-state current is due to diffusion controlled ORR. The diffusion-limited steady current density (i_L) is related to velocity of RDE ($\omega = 2\pi f$, f being the frequency in revolution per second) by Levich equation. The data presented in Fig. 18b suggest that the limiting current is a steady value between -0.47 and -0.6 V at low rpm values of the RDE. A plot of i_L versus $\omega^{1/2}$ is presented in Fig. 18b. The plot is linear suggesting the validity of Eq. (2).

In the limiting current region, current density depends on the rate of diffusion of O_2 across the stagnant layer as described above. This condition prevails in the potential range from -0.40 to -0.47 V (Fig. 18a). However, at low current densities in the potential range, electron-transfer controls the rate of the ORR. In the intermediate range of potential, the reaction is mixed control. In low current region, Koutecky-Levich equation is valid. In Fig. 18 c, i^{-1} versus $\omega^{-1/2}$ plots at different potentials in the range from -0.40 to -0.45 V are presented. The average value of D calculated from the slopes is $1.61 \times 10^{-5} \text{ cm}^2 \text{ s}^{-1}$, which agrees well with the value reported in the literature. In the electron-transfer controlled region, current-potential data were measured potentiostatically while stirring 1 M KOH solution, which was saturated with O_2 gas. The data are presented as Tafel plot in Fig. 18d. The slope of Tafel plot is 75 mV dec^{-1} .

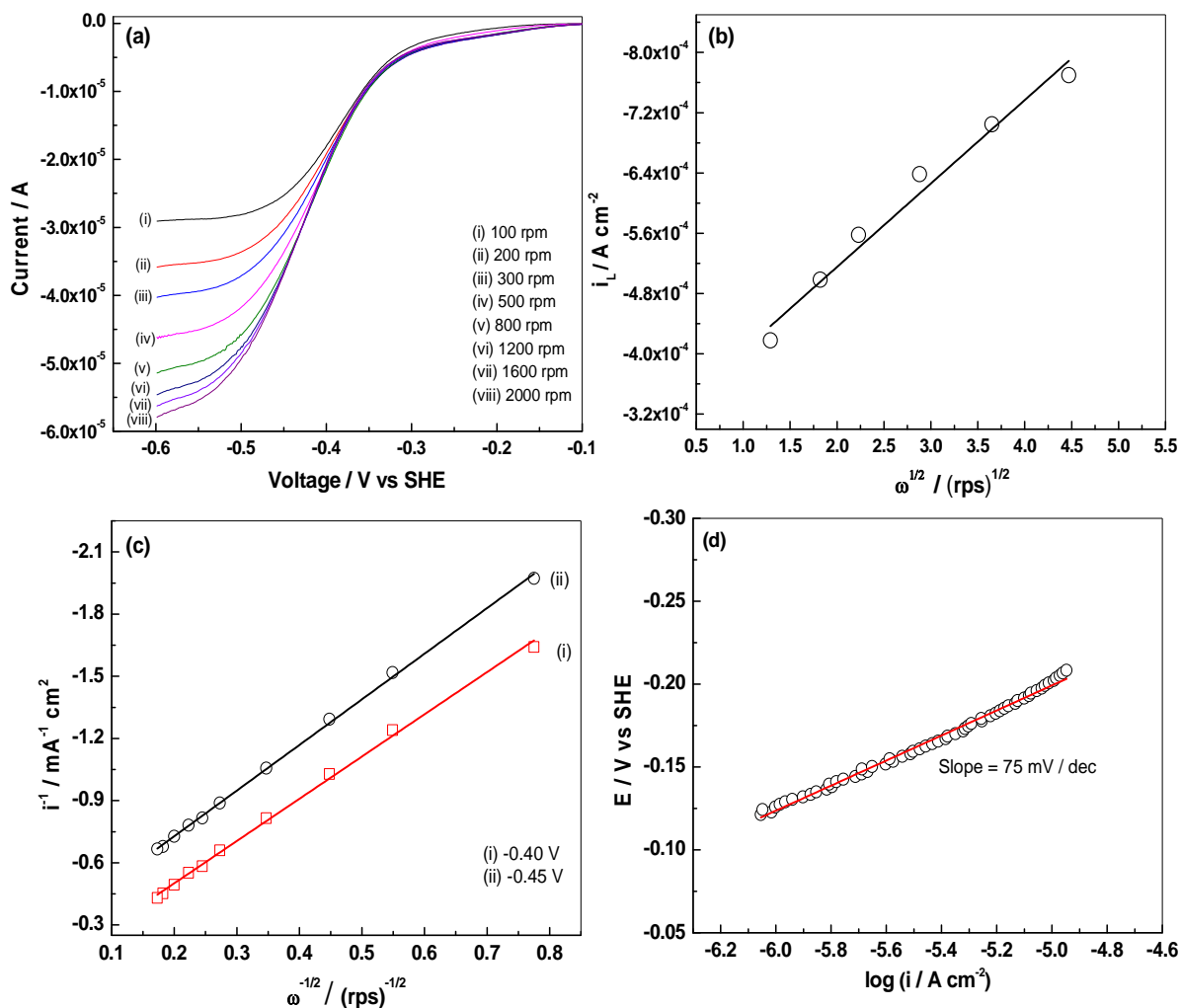


Fig. 18. (a) Linear sweep voltammetry, (b) Levich plot, (c) Koutecky-Levich plot, and (d) Tafel plot for ORR on Au-RGO coated GC electrode in 1 M KOH electrolyte.

3.11. Li-O₂ cell studies using Au-RGO as a catalyst

In the present study, 1.0 M LiPF₆ dissolved in TEGDME is used as the electrolyte and porous Toray carbon paper is used as the current collecting substrate. On one side of the carbon paper, a diffusion-layer made of high surface area ($1500 \text{ cm}^2 \text{ g}^{-1}$) carbon powder with micropores

of diameter less than 2 nm was coated at a loading level of 180 mg cm^{-2} . This side was exposed to O_2 gas. The other side of the carbon paper, which was exposed to the electrolyte, was coated

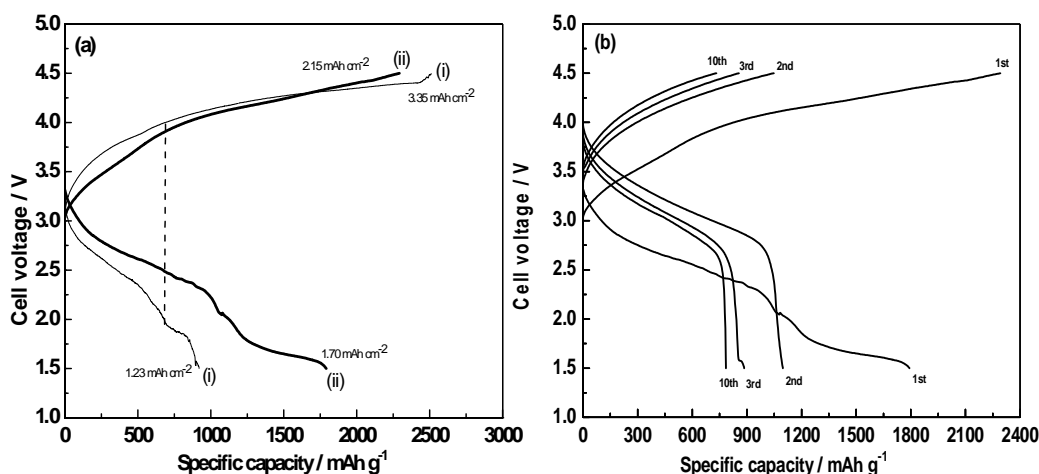


Fig. 19. (a) Charge-discharge profiles $\text{Li-O}_2(\text{RGO})$ (i) and $\text{Li-O}_2(\text{Au-RGO})$ cells at current density 0.3 mA cm^{-2} , (b) charge-discharge voltage profiles of 1st, 2nd, 3rd and 10th cycles of $\text{Li-O}_2(\text{Au-RGO})$ cell at current density of 0.3 mA cm^{-2} .

with the catalyst, namely, Au-RGO. A few cells were assembled with RGO alone for the purpose of comparison. Typical charge-discharge curves of Li-O_2 cells fabricated using RGO and Au-RGO at a current density of 0.3 mA cm^{-2} are presented in Fig. 19a. The open circuit voltage values of freshly assembled cells were 3.00 and 3.25 V for $\text{Li-O}_2(\text{RGO})$ and $\text{Li-O}_2(\text{Au-RGO})$ cells, respectively. Thus, there was an indication for the positive effect of Au present on RGO. On subjecting to discharge at a current density of 0.3 mA cm^{-2} , there is a gradual decrease in voltage of both cells (Fig. 19a). However, the discharge voltage is about 100-200 mV greater for $\text{Li-O}_2(\text{Au-RGO})$ cell than $\text{Li-O}_2(\text{RGO})$ cell. The discharge capacity obtained for $\text{Li-O}_2(\text{RGO})$ cell is about 1348 mAh. On the other hand, it is about 1930 mAh for $\text{Li-O}_2(\text{Au-RGO})$ cell. On the basis of mass of RGO present in $\text{Li-O}_2(\text{RGO})$ cell and Au-RGO present in $\text{Li-O}_2(\text{Au-RGO})$ cell,

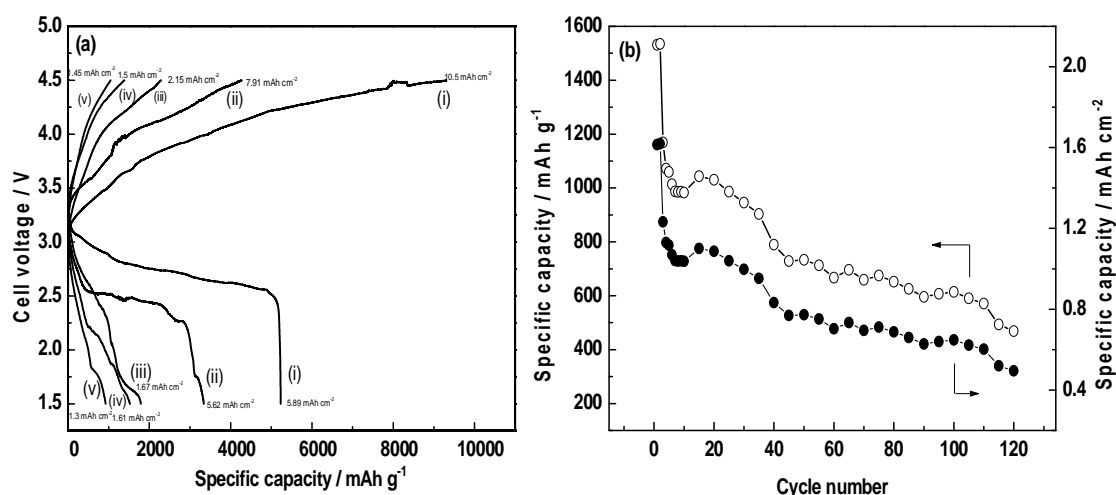


Fig. 20. (a) first discharge curves of Li-O₂(Au-RGO) cells at different currents: (i) 0.1 (ii) 0.2 (iii) 0.3 (iv) 0.6 and (v) 1 mA cm⁻², and (b) cycle-life test of a Li-O₂(Au-RGO) cell at current density of 0.6 mA cm⁻².

the respective specific discharge capacity values become 956 and 1738 mAh g⁻¹. Although the unit of capacity usually reported in the literature for Li-O₂ cells is mAh g⁻¹ on the basis of mass of catalyst loaded carbon, a more appropriate unit is mAh cm⁻². This is because of the fact that carbon or catalyst loaded carbon is not an active material, unlike a battery active material stored within the cell. In the later case, the mass of electrode material generally stored in the cell is used for reporting specific capacity in mAh g⁻¹. In Li-O₂ cells, the mass of O₂ should be used in principle for calculation of specific capacity of the O₂ electrode. Because O₂ is not stored inside the cell, results are generally reported on the basis of mass of the catalyst loaded carbon. The difficulty in using the mass of carbon arises because the loading level of carbon is varied over a wide range in the literature, and capacity is also known to decrease by increasing the mass of carbon. Therefore, the capacity values are additionally reported on the basis of electrode area in mAh cm⁻² in the present work. The discharge specific capacity values of Li-O₂ (RGO) and Li-O₂ (Au-RGO) cells thus are 1.23 mAh cm⁻² (956 mAh g⁻¹) and 1.75 mAh cm⁻² (1738 mAh g⁻¹),

respectively. On charging the cells, the voltage increases gradually up to 4.50 V, but the charging voltage is greater for the Li-O₂(RGO) cell than the Li-O₂(Au-RGO) cell in the initial stages of charging. Thus the difference between the charge voltage and discharge voltage (ΔV) is considerably less for Li-O₂(Au-RGO) cell. For instance, at a capacity of 0.504 mAh cm⁻² (500 mAh g⁻¹), ΔV values are 1.92 and 1.37 V for Li-O₂(RGO) and Li-O₂(Au-RGO) cells, respectively. The lower ΔV value exhibited by Li-O₂(Au-RGO) cell is attributed to the catalytic effect of Au nanoparticles, which are uniformly distributed on RGO layers. The charge capacity values are 3.35 and 2.28 mAh cm⁻² (2613 and 2262 mAh g⁻¹) for Li-O₂(RGO) and Li-O₂(Au-RGO) cells, respectively. Thus, the coulombic efficiency values of charge-discharge cycling, respectively, are 37 % and 76 % for these cells in the first cycle. A comparison of discharge capacity measured in the present study with the values reported in the literature could be inconclusive because there is no uniformity in the literature in experimental conditions such as cell configurations, current collectors, electrodes fabrications, catalysts and their loading levels, electrolytes, current densities (or, specific currents) used for charge-discharge cycling. Nevertheless, 1.75 mAh cm⁻² (1738 mAh g⁻¹) obtained for Li-O₂(Au-RGO) in the present study is a very high value. Charge-discharge voltage profiles of Li-O₂(Au-RGO) cell recorded for repeated cycles are presented in Fig. 19b. There is a decrease in discharge capacity in the 2nd cycle in relation to the first cycle. The discharge voltage plateau increased to a higher level. The end of discharge is indicated by a sharp fall of voltage at about 2.70 V. The charging voltage plateau is also increased for 2nd cycle. The difference between the voltage profile of first and second cycles could be attributed to activation of the cell. The voltage profile from third cycle onwards is similar to the profile of the second cycle.

The existence of a large difference between the charge and discharge voltages of Li-O₂ cells is a serious concern which leads to poor energy efficiency of cycling. The Au-RGO catalyst reduces the magnitude of this difference considerably, thus, confirming an appropriate catalytic activity. Several Li-O₂(Au-RGO) cells were assembled and subjected to charge-discharge cycling with different currents. Charge-discharge curves are presented in Fig. 20a for five different currents. The discharge capacity decreases with an increase in current as expected. The discharge capacity values obtained are 5.89 (5230), 5.62 (3344), 1.75 (1738), 1.61 (1531) and 1.29 mAh cm⁻² (930 mAh g⁻¹), respectively, when discharged at 0.1, 0.2, 0.3, 0.6 and 1.0 mA cm⁻². It is interesting to note that the discharge capacity of 5.89 mAh cm⁻² (5230 mAh g⁻¹) obtained at 0.1 mA cm⁻² is an extremely high value. Furthermore, the discharge voltage profile is flat between 3.00 and 2.75 V at 0.1 mA cm⁻² (Fig. 20a, curve i). There is a decrease in discharge plateau voltage with an increase of current density to 0.2 mA cm⁻² (Fig. 20a curve ii). On further increasing current density to 0.3, 0.6 and 1.0 mA cm⁻², the discharge voltages decrease without any plateaus (Fig. 20a, curves iii, iv and v). The value of 1.29 mAh cm⁻² (930 mAh g⁻¹) obtained at current density as high as 1.0 mA cm⁻² is an attractive value. This indicates high rate capability of Li-O₂(Au-RGO) cells.

Li-O₂(Au-RGO) cells were tested for cycling stability at a current density of 0.6 mA cm⁻² over 120 cycles (Fig. 20b). Initially, about 1.61 mAh cm⁻² (1530 mAh g⁻¹) is obtained. There is a rapid decrease in capacity to about 1.06 mAh cm⁻² (1000 mAh g⁻¹). This is followed by a gradual decrease in capacity. About 0.55 mAh cm⁻² (400 mAh g⁻¹) is obtained for the 120th cycle. When Li-O₂(RGO) cells were cycled, the discharge capacity decreased rapidly in about 5-10 cycles and the cells could not be cycled thereafter. These results confirm the catalytic activity of

Au-RGO for oxygen electrode reaction in non-aqueous rechargeable Li-O₂ cells. Thus, Au-RGO is a promising catalyst for rechargeable Li-O₂ cells.

3.12. Electrochemistry of Pd-RGO catalyst

3.12.1. ORR on Pd-RGO in non-aqueous electrolyte

Cyclic voltammograms of Pd-RGO coated GC electrode recorded at several sweep rates in 0.1 M TBAP-DMSO electrolyte are shown in Fig. 21a. A cathodic current peak appears at -0.98 V in the forward sweep at 10 mV s^{-1} , which is attributed to the reduction of O₂ resulting in the formation of TBAO₂. The anodic peak to the opposite reaction. The cathodic peak current density (i_{pc}) follows Randles – Sevcik equation. A plot of i_{pc} versus $v^{1/2}$ is a straight line (Fig. 21b) indicating the ORR is controlled by diffusion of O₂. Similar observation is made for the anodic peak current density (i_{pa}) also from i_{pa} versus $v^{1/2}$ data (Fig. 21b).

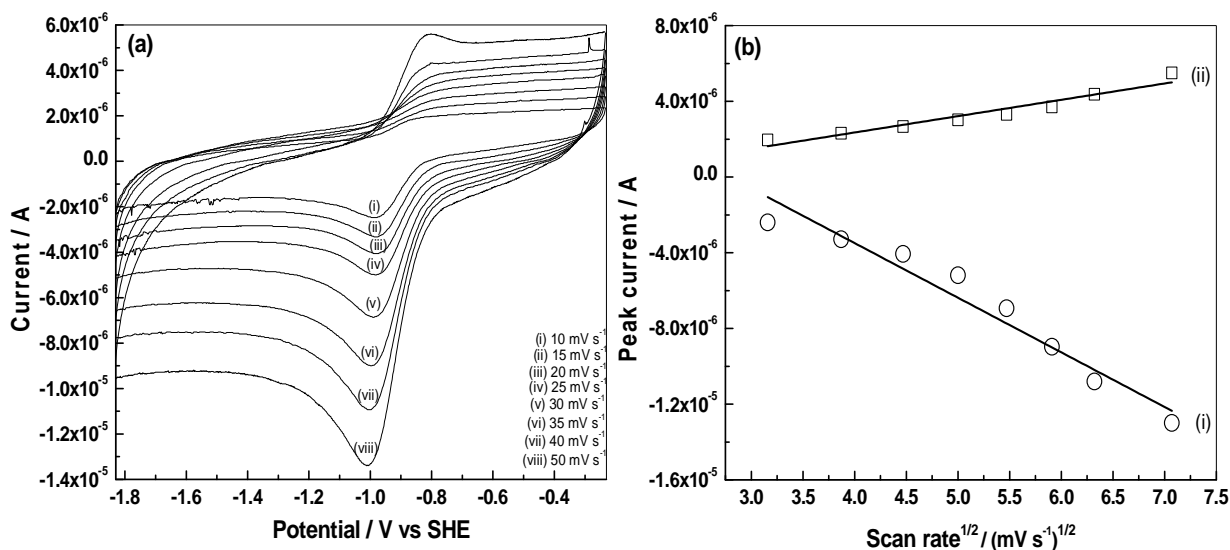


Fig. 21. (a) Cyclic Voltammograms of Pd-RGO for ORR activity at different scan rates and (b) plot between peaks current versus (scan rate)^{1/2} in 0.1M TBAP-DMSO.

Linear sweep voltammograms recorded in O₂ saturated 0.1 M TBAP-DMSO solution at several rotation speeds of RDE are presented in Fig. 22a. The voltammograms (Fig. 22a) are characterized by electron-transfer controlled regime in potential range from -0.70 to -1.20 V and diffusion-controlled regime with limiting current in the potential range from -1.30 to -1.83 V and a mixed regime in between. A plot of limiting current density measured at -1.60 V versus $\omega^{1/2}$ is linear (Fig. 22b) suggesting the validity of eqn. 2 for ORR in the non-aqueous electrolyte also. The value of D obtained is $1.62 \times 10^{-6} \text{ cm}^2 \text{ s}^{-1}$.

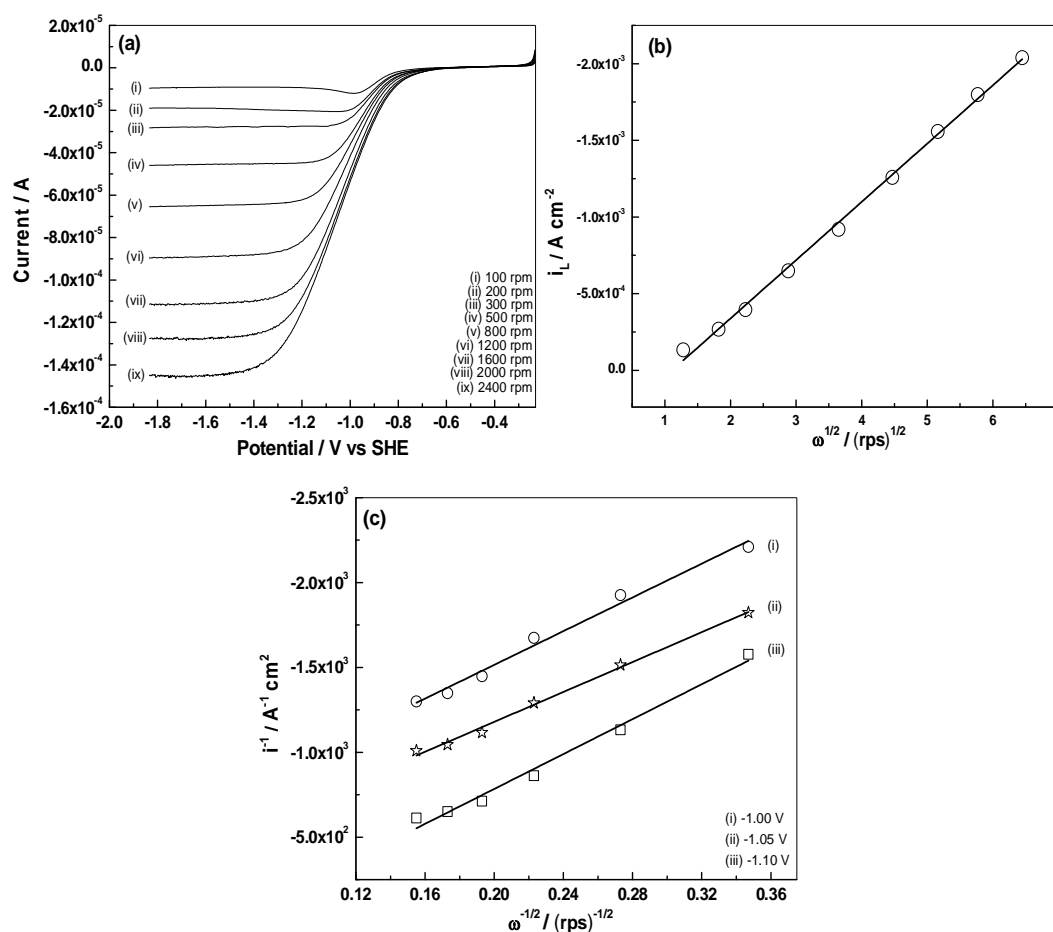


Fig. 22. (a) linear sweep voltammograms at 10 mV s^{-1} with different speeds (rpm) of rotation in 0.1M TBAP-DMSO, (b) Levich plot at -1.60 V, and (c) Koutecky-Levich plots. The area of GC electrode is 0.0314 cm^2 with catalyst mass of $200 \mu\text{g}$.

The Koutecky – Levich plots (Fig. 22c) constructed at several potentials in the mixed potential regime are linear. The average value of n calculated is 0.85, which is close to unity. It is thus inferred that the formation of superoxide (O_2^-) in the non-aqueous electrolyte is the rate determining steps.

3.12.2. Li-O₂ cell studies using Pd-RGO as a catalyst

Several cells were assembled and tested for Li-air study using Pd-RGO. Fig. 23a shows the charge discharge voltage curves of Li-air cells cycled at the different current densities. Specific capacity values of the cells are 8192 (13.58), 6243 (10.30), and 2138 mAh g⁻¹ (4.13 mAh cm⁻²), at specific current density of 0.2, 0.5, and 0.8 mA cm⁻² respectively. At 0.2 mA cm⁻², discharge plateau appeared at 2.7 V and the charge plateau at 4.2 V. The voltage difference between charge and discharge curves is more than 1 V. When the current density is increased to 0.5 and 0.8 mA cm⁻², there is a decrease in discharge voltage, while charge voltage is increased due to high polarization at the air electrode. The specific capacity of the cells also decreased. A comparison of discharge capacity obtained in the present study with the values reported in the literature could be inconclusive because there is no uniformity in experimental conditions such as cell configurations, current collectors, electrodes fabrication, nature of the catalyst and its loading level, electrolytes, current densities used for charge-discharge cycling, etc. Li-O₂ cells were tested for cycling stability at a current density of 0.5 mA cm⁻² over 30 cycles (Fig. 23c). Initially, about 6244 mAh g⁻¹ (10.30 mAh cm⁻²) is obtained. There is a rapid decrease in capacity to 3600 mAh g⁻¹ (5.94 mAh cm⁻²) at 5th Cycle. This was followed by a gradual decrease in capacity. The discharge capacity 523 mAh g⁻¹ (0.86 mAh cm⁻²) is obtained for the 25th cycle.

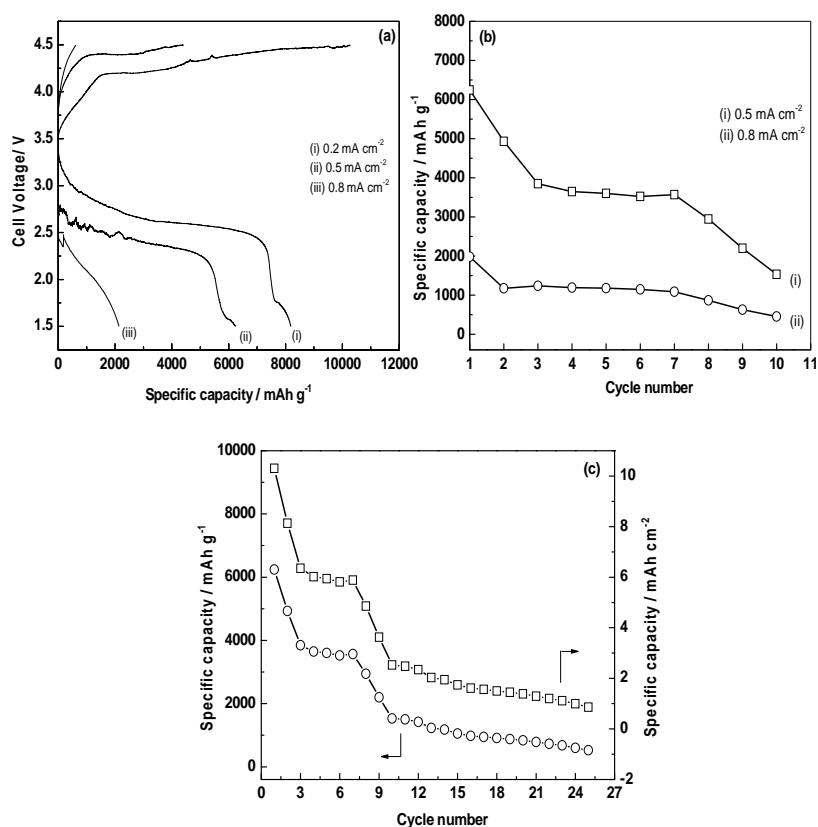


Fig. 23(a) Charge-discharge curves of first cycle at different current densities, (b) comparison of discharge capacities at 0.5 and 0.8 mA cm⁻², and (c) cycle life test at current density 0.5 mA cm⁻².

3.13. Electrochemistry of Ir-RGO

3.13.1. ORR on Ir-RGO in 1 M KOH electrolyte

Linear sweep voltammograms of Ir-RGO coated GC RDE were recorded at a sweep rate of 10 mV s⁻¹ with different speeds in 1M KOH solution saturated with O₂ (Fig. 24a). At all speeds of RDE, current is negligibly small between 0.30 and 0.07 V. The reduction current starts increasing at 0.07 V. Current between 0.07 to -0.10 V is due to mixed control. The steady-state current in the potential range more negative to -0.10 V is due to diffusion controlled ORR. The

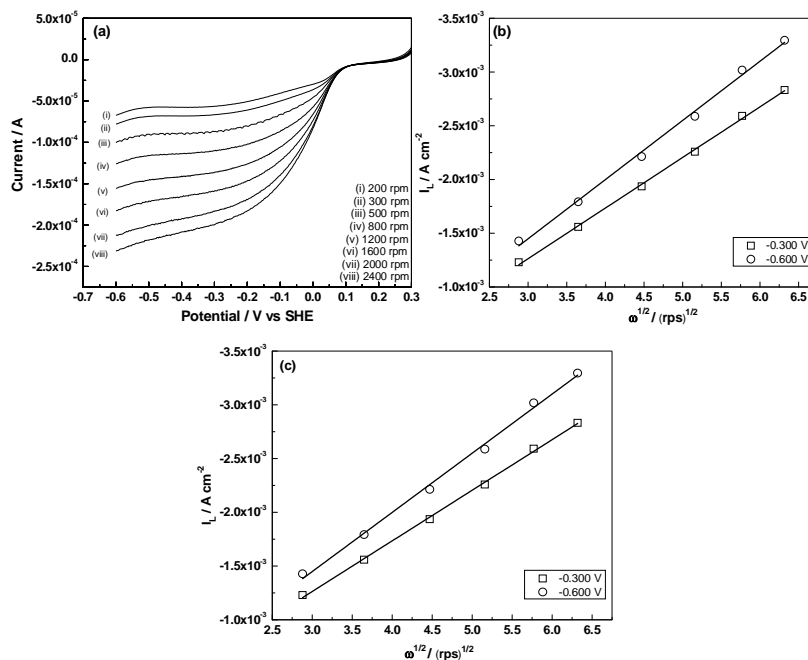


Fig. 24. (a) Linear sweep voltammetry of Ir-RGO for ORR at 10 mVs^{-1} after saturation with O_2 gas in 1M KOH in different rotation speeds, (b) Levich plot, and (c) Koutecky-Levich plot. The area of GC electrode is 0.0314 cm^2 with catalyst mass of $200 \text{ }\mu\text{g}$.

data presented in Fig. 24a suggest that the limiting current is a steady value between -0.10 and -0.60 V . A plot of i_L versus $\omega^{1/2}$ (Fig. 24b) is linear suggesting the validity of Levich equation. The number of electrons involved in oxygen reduction is calculated as 3.18. However, at low current densities in the potential range 0.30 to -0.07 V , electron-transfer controls the rate of the ORR. In the intermediate range of potential (-0.07 to -0.10 V), the reaction is mixed control and Koutecky-Levich equation is valid. A plot of i^{-1} versus $\omega^{-1/2}$ is expected to be linear. Plots of i^{-1} versus $\omega^{-1/2}$ at different potentials in the range from -0.07 to -0.10 V are presented in Fig. 24c. The average value of D calculated from the slopes is $1.82 \times 10^{-5} \text{ cm}^2 \text{ s}^{-1}$, which agrees well with the value calculated reported in the literature.⁴⁴ In the electron-transfer controlled region, current-potential data were measured potentiostatically while stirring 1M KOH solution, which was

saturated with O₂ gas. The values of k obtained from the intercepts (Fig. 24c) are in the range 6.5 to 1.96 cm² s⁻¹.

3.13.2. ORR on Ir-RGO in non-aqueous electrolyte

Cyclic voltammograms of Ir-RGO coated GC electrode recorded at several sweep rates in 0.1 M TBAP-DMSO electrolyte are shown in Fig. 25a. A cathodic current peak appears at -0.93 V in the forward sweep at 10 mV s⁻¹, which is attributed to the reduction of O₂ resulting in the formation of TBAO₂. The cathodic current peak (P_c) in Fig. 25a. is attributed to reduction of O₂ (reaction 4) and the anodic peak (P_a) to the opposite reaction. As the anodic charge is nearly equal to the cathodic charge, it is inferred that oxygen reaction is highly reversible in the non-aqueous electrolyte. The cathodic peak current density (i_{pc}) follows Randles-Sevcik equation (Eq. 6). A plot of i_{pc} versus v^{1/2} is a straight line (Fig. 25b) indicating the ORR is controlled by diffusion of O₂. Similar observation is made for the anodic peak current density (i_{pa}) also from i_{pa} versus v^{1/2} data (Fig. 25b).

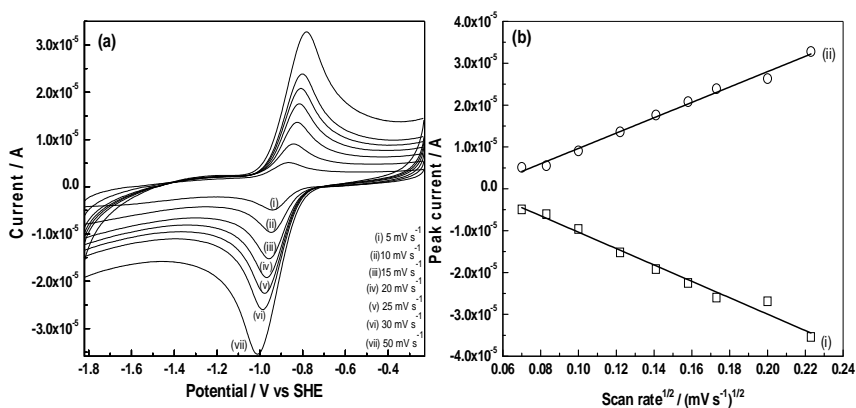


Fig. 25. (a) Cyclic Voltammograms of Ir-RGO for ORR activity at different scan rates and (b) plot between peaks current versus (scan rate)^{1/2} in 0.1M TBAP-DMSO.

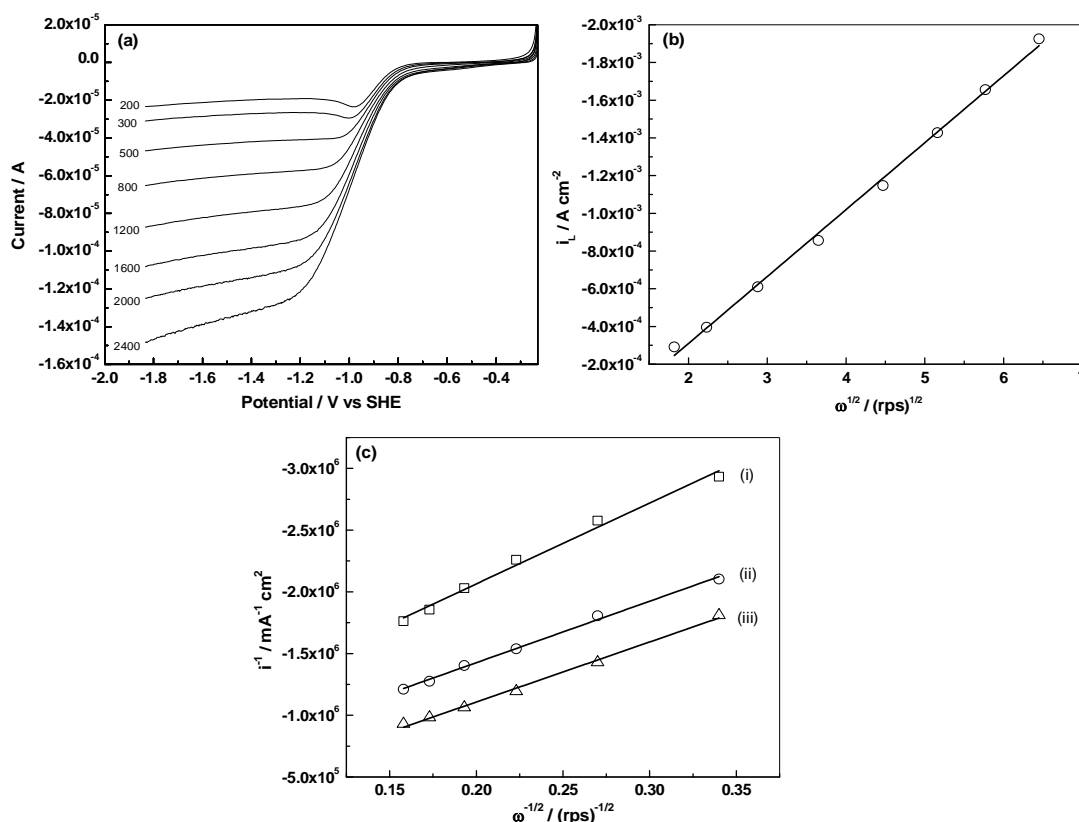


Fig. 26. (a) linear sweep voltammograms at 10 mV s^{-1} with different speeds (rpm) of rotation in 0.1M TBAP-DMSO, (b) Levich plot at -1.60 V , and (c) Koutecky-Levich plots at -0.92 V (i), -0.97 V (ii) and -1.02 V (iii). The area of GC electrode is 0.0314 cm^2 with catalyst mass of $200 \mu\text{g}$.

Linear sweep voltammograms recorded in O_2 saturated 0.1 M TBAP-DMSO solution at several rotation speeds of RDE are presented in Fig. 26a. The voltammograms (Fig. 26a) are characterized by electron-transfer controlled regime in potential range from -0.23 to -0.72 V diffusion-controlled regime with limiting current in the potential range from -1.20 to -1.90 V and a mixed regime in between. A plot of limiting current density measured at -1.60 V versus $\omega^{1/2}$ is linear (Fig. 26b) suggesting the validity of eqn. 2 for ORR in the non-aqueous electrolyte also. The value of D obtained is $1.62 \times 10^{-6} \text{ cm}^2 \text{ s}^{-1}$. The Koutecky-Levich plots (Fig. 26c) constructed at several potentials in the mixed potential regime are linear. The average value of n calculated is

0.85, which is close to unity. It is thus inferred that the formation of superoxide (O_2^-) in the non-aqueous electrolyte is the rate determining steps.

3.14. Li-O₂ cell studies using Ir-RGO catalyst

Fig. 27 shows the charge discharge voltage curves of Li-air cells cycled at the different current densities. Specific capacity values of the cells for first cycle are 11449 (12.24), 9529 (11.36), and 6162 mAh g⁻¹ (6.73 mAh cm⁻²), at specific current density of 0.2, 0.5, and 0.8 mA cm⁻² respectively. At 0.2 mA cm⁻², discharge plateau appeared at 2.7 V and the charge plateau at 4.2 V. The voltage difference between charge and discharge curves is more than 1 V. When the current density is increased to 0.5 and 0.8 mA cm⁻², there is a decrease in discharge voltage, while charge voltage is increased due to high polarization at the air electrode. The specific capacity of the cells also decreased.

Li-O₂ cells were tested for cycling stability at a current density of 0.5 mA cm⁻² over 30 cycles (Fig. 27b). Initially, about 9529 mAh g⁻¹ (11.36 mAh cm⁻²) is obtained. There is a rapid decrease

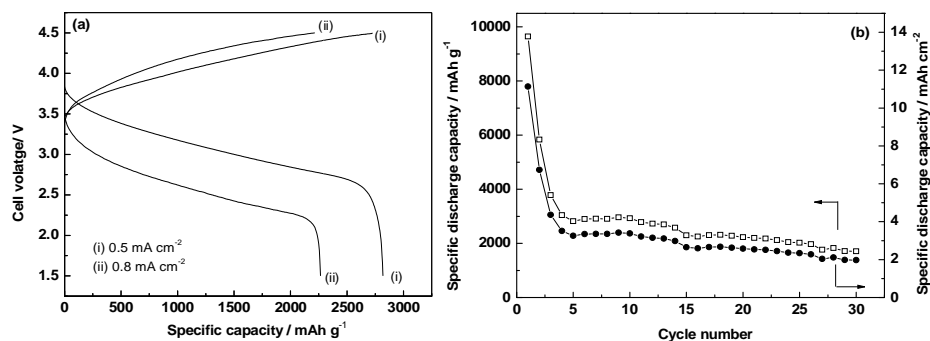


Fig.27. Charge-discharge curves of 5th cycle at different current densities, and (b) cycle life test at current density 0.5 mA cm⁻².

in capacity to 2822 mAh g⁻¹ (3.25 mAh cm⁻²) at 5th Cycle. This was followed by a gradual decrease in capacity. The discharge capacity 1710 mAh g⁻¹ (1.97 mAh cm⁻²) is obtained for the 30th cycle. When Li-O₂(RGO) cells were cycled, the discharge capacity decreased rapidly in about 5-10 cycles and the cells could not be cycled thereafter. These results confirm the catalytic activity of Ir-RGO for oxygen electrode reaction in non-aqueous rechargeable Li-O₂ cells.

3.15. Li-O₂ cell studies using PPY-RGO catalyst

Li-O₂ cells made of RGO and RGO-PPY were subjected to charge-discharge cycling at a current density of 0.3 mA cm⁻² between 1.50 and 4.50 V, for comparison. The variation of cell voltage during discharge and charge processes of the first cycle is shown in Fig. 28a. The cell voltage decreases gradually initially during the discharge, reaches a plateau and falls sharply at the end of discharge. The discharge plateau voltage for Li-O₂ (RGO-PPY) cell is about 2.50 V. During the charging process, the cell voltage increases gradually up to 4.50 V. The discharge and charge capacity values of the Li-O₂ (RGO-PPY) cell are 3358 mAh g⁻¹ (3.94 mAh cm⁻²) and 5262 mAh g⁻¹ (5.5 mAh cm⁻²), respectively, for the first cycle. The discharge capacity of the second cycle obtained is 2171 mAh g⁻¹ (2.55 mAh cm⁻²). For the Li-O₂ (RGO) cell, the discharge capacity is 911 mAh g⁻¹ (1.23 mAh cm⁻²) which is considerably less than 3358 mAh g⁻¹ (3.94 mAh cm⁻²) obtained for the Li-O₂(RGO-PPY) cell. This corresponds to about 3.7 times greater discharge capacity of Li-O₂(RGO-PPY) cell in relation to Li-O₂(RGO) cells. In view of the difference in specific BET area values of RGO-PPY (250 m² g⁻¹) and RGO (401 m² g⁻¹), the relative discharge capacities of the two cells can also be compared on the basis of area.

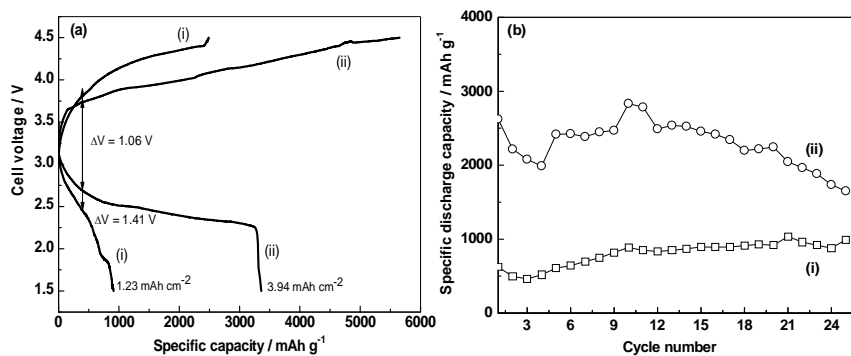


Fig. 28. (a) Discharge and charge curves of Li-O₂(RGO) (i) and Li-O₂(RGO-PPY) (ii) cells at current density of 0.3 mA cm⁻² and (b) variation of specific capacities of Li-O₂(RGO) (i) and Li-O₂(RGO-PPY) (ii) cells at a current density of 0.5 mA cm⁻².

Taking account of ratio (0.62) of surface area values of RGO-PPY and PPY, the enhancement in discharge capacity of Li-O₂(RGO-PPY) cell is about 2.3 times of the capacity of Li-O₂(RGO) cell. Thus, the increase in capacity is attributed to the presence of PPY in Li-O₂(RGO-PPY) cells. Furthermore, the difference in voltages (ΔV) between charge and discharge is also smaller for Li-O₂(RGO-PPY) cell than for Li-O₂(RGO) cell. For instance, at a capacity of 50 mAh g⁻¹, the values of ΔV are 1.06 and 1.41 V for Li-O₂(RGO-PPY) and Li-O₂(RGO) cells, respectively. Thus, RGO-PPY is a more efficient catalyst than RGO for oxygen reduction in Li-O₂ cell environment.

Li-O₂(RGO-PPY) and Li-O₂(RGO) cells were subjected to continuous charge-discharge cycles at 0.5 mA cm⁻² (Fig. 28b). The discharge capacity of the former cell is greater than the latter throughout the cycle-life test. Nevertheless, a discharge capacity of 3358 mAh g⁻¹ (3.94 mAh cm⁻²) obtained for Li-O₂(RGO-PPY) cell is an attractively high value.

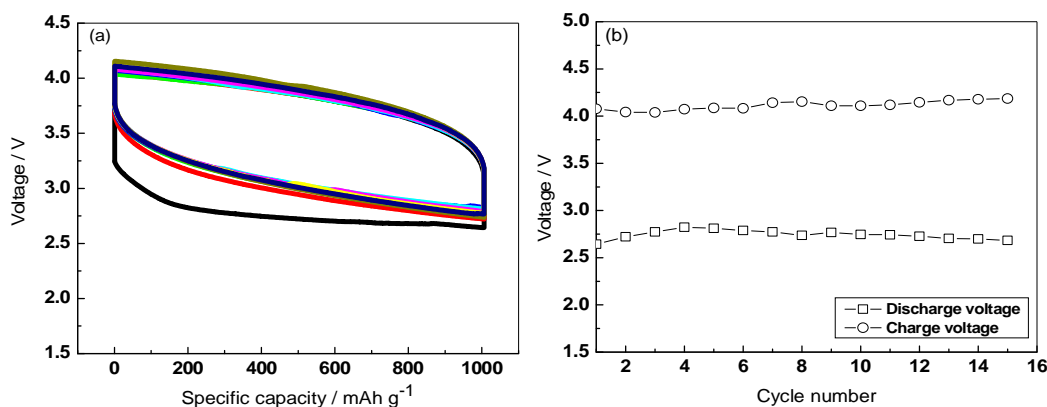


Fig. 29. (a) Discharge-charge performance of Li-O₂(RGO-PPY) cell with a current density of 0.2 mA cm⁻² limiting to a capacity of 1000 mAh g⁻¹ and (b) variation of cut-off voltages on cycling.

Cycling stability of Li-O₂(RGO-PPY) cell was tested by subjecting the cell to discharge and charge cycles limiting the capacity to 1000 mAh g⁻¹ (Fig. 29a). The first discharge curve exhibits a lower voltage than the subsequent cycles. The discharge and charge curves for the next 14 cycles are merged (Fig. 29a). The cell voltage values at the end of discharge and at the end of charge (Fig. 29b) are constant at 2.75 and 4.10 V, respectively. These features indicate the electrochemical stability of the RGO-PPY catalyst and also Li-O₂ cells.

Several cells of Li-O₂(RGO-PPY) were assembled and subjected to discharge-charge cycling at different current densities in the range from 0.2 to 1.0 mA cm⁻². The variations of discharge capacity with current density are shown in Fig. 30a. There is a decrease in discharge capacity with an increase in current density, as expected.

A few Li-O₂(RGO-PPY) cells were subjected to cycle-life test with different current densities (Fig. 30b). The discharge capacity decreases in the first few cycles and thereafter it remains fairly constant, when cycled at 0.6 and 0.7 mA cm⁻². At 1.0 mA cm⁻², however, the initial discharge capacity is about 550 mAh g⁻¹ (0.43 mAh cm⁻²) and the Li-O₂(RGO-PPY) cell shows an increasing tendency of the discharge capacity. The values of discharge capacity

obtained for the 30th cycle are 1500 (1.27 mAh cm⁻²), 1015 (0.93 mAh cm⁻²) and 961 mAh g⁻¹ (0.75 mAh

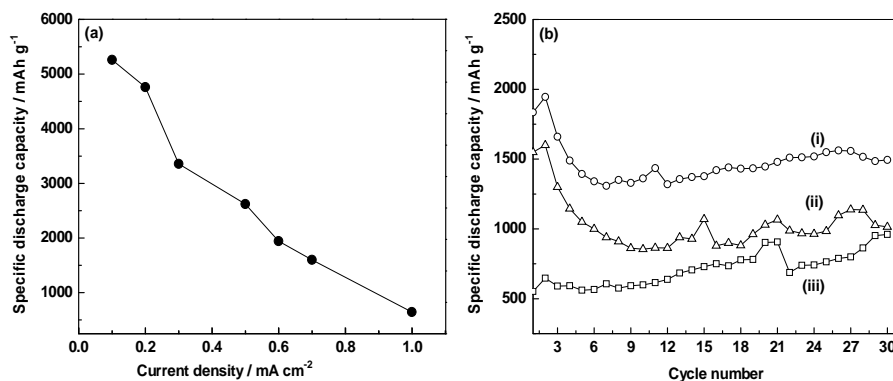


Fig. 30. (a) Variation of specific discharge capacity of Li-O₂(RGO-PPY) cell when cycled at different current densities and (b) discharge capacities of Li-O₂(RGO-PPY) cells as a function of cycle number when cycled with current density of 0.6 (i), 0.7 (ii) and 1.0 mA cm⁻² (iii).

cm⁻²), respectively, for 0.6, 0.7 and 1.0 mA cm⁻² current densities. Current density of 1.0 mA cm⁻² used for charge-discharge cycling is considered high for Li-O₂ cells. At this high current density, a reasonably high value of discharge capacity is obtained (Fig. 30b).

4. CONCLUSIONS

Several catalysts on the basis of graphene (or, reduced graphene oxide, RGO) are prepared and studied for their activity towards oxygen electrode reaction in Li-O₂ cells. The in situ preparation of Ag-RGO, Au-RGO, Pd-RGO and Ir-RGO facilitate formation of metal nanoparticles anchored to RGO nanosheets. Additionally, PPY-RGO is also prepared by physical mixing. All catalysts are characterized for their physical properties and microstructure. Electrochemical characterization and performance of Li-O₂ cells are summarized in the table given below.

Catalyst	Ag-RGO	Au-RGO	Pd-RGO	Ir-RGO	PPY-RGO
Particle size / nm	4.70	5.20	3.50	3.90	-----
Electrolyte used for CV/RDE study	0.1 M TBAP-DMSO	0.1 M TBAP-DMSO	0.1 M TBAP-DMSO	0.1 M TBAP-DMSO	-----
Number of electron involved for ORR	0.70	0.80	0.85	0.85	-----
Electrolyte for Li-O ₂ cell	LiPF ₆ -DMSO	LiPF ₆ -TEGDME	LiPF ₆ -DMSO	LiPF ₆ -DMSO	LiPF ₆ -TEGDME
Discharge capacity at 0.2 mA (1 st cycle)	11 950	3344	8192	11449	4763
Discharge capacity at 0.2 mA (10 th cycle)	788 (6.6%)* I	728 (21.8%)* III	1120 (13.7%)* II	3692 (32.3%)* IV	1857 (39.0%)* V
Discharge capacity at 0.2 mA (30 th cycle)	345 (2.9%)* I	695 (20.8%)* V	318 (3.9%)* II	1583 (13.8%)* III	693 (14.5%)* IV
Discharge capacity at 0.5 mA (1 st cycle)	9340	1658	6243	9529	2622
Discharge capacity at 0.5 mA (10 th cycle)	1720 (18.4%)* I	862 (52.0%)* IV	1531 (34.5%)* III	2931 (30.8%)* II	1478 (56.4%)* V
Discharge capacity at 0.5 mA (30 th cycle)	534 (5.7%)* I	467 (28.2%)* V	523 (8.4%)* II	1710 (17.9%)* III	635 (24.2%)* IV
Discharge capacity at 0.8 mA (1 st cycle)	2780	1296	2138	6162	1562
Discharge capacity at 0.8 mA (10 th cycle)	824 (29.6%)* IV	708 (54.6%)* III	452 (21.1%)* I	1917 (31.1%)* II	906 (58.0%)* V
Discharge capacity at 0.8 mA (30 th cycle)	586 (21.1%)* II	301 (23.2%)* IV	221 (10.3%)* I	1402 (22.8%)* III	674 (43.1%)* V

Table: Comparison of performance of catalysts

*Capacity retention as percent of the first cycle capacity. Increasing order of capacity retention is indicated by I to V

It is seen in the Table above that Ag-RGO and Ir-RGO provide high initial discharge capacity, but the capacity retention is poor. From the capacity retention view point, PPY-RGO and Au-RGO are better. As the adsorption of O₂ on the catalyst is a primary step for its reduction, different catalyst materials possess different catalytic activity. Accordingly, there are differences in the discharge capacity values. A large difference in plateau potentials of discharge and charge is a serious problem in Li-O₂ cells, and this feature is present in the present studied also. Additional investigations are necessary for addressing this problem

References

1. K. M. Abraham and Z. Jiang, *J. Electrochem. Soc.*, 1996, **143**, 1-5.
2. G. Girish Kumar, B. McCloskey, A. C. Luntz, S. Swanson and W. Wilcke, *J. Phys. Chem. Lett.*, 2010, **1**, 2193-2203.
3. S. D. Beattie, D. M. Manolescu and S. L. Blair, *J. Electrochem. Soc.*, 2009, **156**, A44-A47.
4. T. Ogasawara, A. Debart, M. Holzapfel, P. Novak and P. G. Bruce, *A. Am. Chem. Soc.*, 2006, **128**, 1390-1393.
5. A. Debart, A. J. Paterson, J. Bao and P. G. Bruce, *Angew, Chem. Int. Ed.*, 2008, **47**, 1-5.
6. Y-C Lu, Z. Xu, H. A. Gasteiger, S. Chen, K. Hamad-Schifferli, and Y. Shao-Horn, *J. Am. Chem. Soc.*, 2010, **132**, 12170-12171.
7. L. Wang, X. Zhao, Y. Lu, M. Xu, D. Zhang, R. S. Ruoff, K. J. Stevenson and J. B.

- Goodenough, *J. Electrochem. Soc.*, 2011, **158**, A1379-A1382.
8. Y. Li, J. Wang, X. Li, D. Geng, R. Li and X. Sun, *Chem. Comm.*, 2011, **47**, 9438-9440.
9. E. Yoo and H. Zhou, *ACS Nano*, 2011, **5**, 3020-3026.
10. A. K. Geim and K. S. Novoselov, *Nature Mater.*, 2007, **6**, 183-191.
11. Z. Peng, S. A. Freunberger, Y. Chen and P. G. Bruce, *Science*, 2012, **337**, 563-566.
12. W. S. Hummers Jr. and R. E. Offeman, *J. Am. Chem. Soc.*, 1958, **80**, 1339.
13. M. Eswaran, N. Munichandraiah and L. G. Scanlon, *Electrochem. Solid-State Lett.*, 2010, **13**, A121-A124.
14. C. Selvaraj, N. Munichandraiah and L. G. Scanlon, *J. Porphyrins Phthalocyanines*, 2012, **16**, 255-259.
15. J. Shen, Y. Hu, M. Shi, X. Lu, C. Qin and C. Li, *Chem. Mater.*, 2009, **21**, 3514-3520.
16. S. Dubin, S. Gilje, K. Wang, V.C. Tung, K. Cha, A.S. Hall, J. Farrar, R. Varshneya and Y. Yang and R. B. Kaner, *ACS Nano*, 2010, **4**, 2845-3852.
17. Z. Sun, Z. Yan, J. Yao, E. Beitler, Y. Zhu and J. M. Tour, *Nature*, 2010, **468**, 549-552.
18. S. D. Beattie, D. M. Monlescu and S. L. Blair, *J. Electrochem. Soc.*, 2009, **156**, A44-A47.
19. C. O. Laoire, S. Mukerjee and K. M. Abraham, *J. Phys. Chem. C.*, 2009, **113**, 20127-20137.
20. S. A. Freunberge, Y. Chen, Z. Pneg, J. M. Griffin, L. J. Hard-wick, F. Bard, P. Novak and P. G. Bruce, *J. Am. Chem. Soc.*, 2011, **133**, 8040-8047.
21. S. A. Freunberger, Y. Chen, N. E. Drewett, L. J. Hardwick, F. Barde and P. G.

- Bruce, *Angew. Chem. Int. Ed.*, 2011, **50**, 8609-8613.
22. D. Sharon, V. Etacheri, A. Garsuch, M. Afri, A. A. Frimer and D. Aurbach, *J. Phys. Chem. Lett.*, 2013, **4**, 127-131.
23. S. Kumar, C. Selvaraj, N. Munichandraiah and L. G. Scanlon, *RSC Adv.*, 2013, **3**, 21706–21714.
24. C. Selvaraj, S. Kumar, N. Munichandraiah and L. G. Scanlon, *J. Electrochem. Soc.*, 2014, **161**, A554-A560.
25. S. Kumar, C. Selvaraj, L. G. Scanlon and N. Munichandraiah, *Phys. Chem. Chem. Phys.*, 2014, **16**, 22830-22840.

Acknowledgements:

We thank the Asian Office of Aerospace Research and Development of the U.S. Air Force for their financial support vide contract No. FA4869-07-1-4090 and FA2386-10-1-4093. Also, we thank Dr. L.G. Scanlon, Dt. Tammy Low, Dr. Pon, Dr. Ashok S. Patil and other officials for their interest in this work and for helpful discussions.